

Phospholipid peroxidation in macrophage confers tumor resistance by suppressing phagocytic capability towards ferroptotic cells

Rong-Rong He (✉ rongronghe@jnu.edu.cn)

Jinan University <https://orcid.org/0000-0001-5505-5672>

Xiang Luo

International Cooperative Laboratory of Traditional Chinese Medicine Modernization and Innovative Drug Development of Chinese Ministry of Education (MOE), College of Pharmacy, Jinan University

Zi-Chun Li

Jinan University

Dong-Dong Li

Jinan University

Zi-Xuan Li

Jinan University

Hai-Biao Gong

Jinan University

Chang-Yu Yan

Jinan University

Rui-Ting Huang

Macau University of Science and Technology

Yue Feng

Jinan University

Shurui Chen

First Affiliated Hospital of Jinzhou Medical University

Yun-Feng Cao

National Health Commission Key Laboratory of Reproduction Regulation, Shanghai, China

Mingxian Liu

Jinan University

Rong Wang

Jinan University

Feng Huang

Yunnan University

Wan-Yang Sun

Jinan University

Hiroshi Kurihara

Institute of Traditional Chinese Medicine & Natural Products, Pharmacy College, Jinan University,
Guangzhou 510632, China

Wen-Jun Duan

Jinan University <https://orcid.org/0000-0001-7324-9526>

Lei Liang

Jinan University

Wen Jin

Jinan University

Yi-Fang Li

Jinan University

Yan-Ping Wu

Jinan University

Article**Keywords:**

Posted Date: October 19th, 2023

DOI: <https://doi.org/10.21203/rs.3.rs-3396037/v1>

License:  This work is licensed under a Creative Commons Attribution 4.0 International License.

[Read Full License](#)

Additional Declarations: There is no duality of interest

Phospholipid peroxidation in macrophage confers tumor resistance by suppressing phagocytic capability towards ferroptotic cells

Xiang Luo¹, Zi-Chun Li¹, Dong-Dong Li¹, Zi-Xuan Li¹, Hai-Biao Gong¹, Chang-Yu Yan¹, Rui-Ting Huang², Yue Feng³, Shu-Rui Chen¹, Yun-Feng Cao⁴, Mingxian Liu³, Rong Wang^{1,5}, Feng Huang⁵, Wang Yang Sun¹, Hiroshi Kurihara¹, Wen-Jun Duan¹, Lei Liang¹, Wen Jin¹, Yi-Fang Li¹✉, Yan-Ping Wu¹✉, Rong-Rong He^{1,2,5}✉

¹Guangdong Second Provincial General Hospital/Guangdong Engineering Research Center of Chinese Medicine & Disease Susceptibility/International Cooperative Laboratory of Traditional Chinese Medicine Modernization and Innovative Drug Development of Chinese Ministry of Education (MOE)/Guangdong Province Key Laboratory of Pharmacodynamic Constituents of TCM and New Drugs Research/Integrated Chinese and Western Medicine Postdoctoral Research Station, Jinan University, Guangzhou 510632, China

²State Key Laboratory of Quality Research in Chinese Medicine, Macau University of Science and Technology, Macau 999078, China

³Department of Materials Science and Engineering, College of Chemistry and Materials Science, Jinan University, Guangzhou 511443, China

⁴Shanghai Institute for Biomedical and Pharmaceutical Technologies, National Health Commission Key Laboratory of Reproduction Regulation, Shanghai, China

⁵School of Chinese Materia Medica and Yunnan Key Laboratory of Southern Medicinal Utilization, Yunnan University of Chinese Medicine, Kunming 650500, China

✉email: rongronghe@jnu.edu.cn; wuyanping@jnu.edu.cn; liyifang706@jnu.edu.cn

37 **Abstract:**

38 Ferroptosis holds significant potential for application in cancer therapy. However, ferroptosis inducers
39 are not well cell-specific and can cause phospholipid peroxidation in both tumor and non-tumor cells.
40 This limitation greatly restricts the use of ferroptosis therapy as a safe and effective anticancer strategy.
41 Our previous study demonstrated that macrophages can engulf ferroptotic cells through Toll-like
42 receptor 2 (TLR2). Despite this advancement, the precise mechanism by which phospholipid
43 peroxidation in macrophages affects their phagocytotic prowess during treatment of tumors with
44 ferroptotic agents is still unknown. Here, we determined that phospholipid peroxidation in macrophages
45 impaired their ability to eliminate ferroptotic tumor cells by phagocytosis, ultimately fostering tumor
46 resistance to ferroptosis therapy. Mechanistically, the accumulation of phospholipid peroxidation in the
47 macrophage endoplasmic reticulum (ER) repressed TLR2 trafficking to plasma membrane and caused
48 its retention in the ER by disrupting the interaction between TLR2 and its chaperone CNPY3.
49 Subsequently, this ER-retained TLR2 recruited E3 ligase MARCH6 and initiated the proteasome-
50 dependent degradation. Using phospholipidomics, we identified 1-stearoyl-2-15-HpETE-sn-glycero-3-
51 phosphatidylethanolamine (SAPE-OOH) as the crucial mediator of these effects. Conclusively, this
52 discovery elucidates a novel molecular mechanism underlying macrophage phospholipid peroxidation-
53 induced tumor resistance to ferroptosis therapy and highlights the TLR2-MARCH6 axis as a potential
54 therapeutic target for cancer therapy.

55
56
57
58
59
60
61
62
63
64
65
66

67 **Introduction**

68 Ferroptosis, a form of cell death that is driven by iron-dependent accumulation of phospholipid
69 peroxides, has emerged as a promising avenue for innovative cancer therapy [1, 2]. However, despite
70 its potential, the broad application of ferroptosis-inducing agents in clinical settings has been hindered
71 by a significant challenge: the lack of cell specificity, resulting in unintended phospholipid peroxidation
72 in all cells in the tumor microenvironment (TME). This intrinsic limitation poses a significant challenge
73 to the feasibility of ferroptosis-based anticancer strategies.

74 Macrophages, being the most abundant immune cell population in the TME, are crucial for tumor
75 immunosurveillance [3, 4]. Phagocytosis is particularly important for removing dying tumor cells
76 during cancer therapy [5, 6]. Effective phagocytosis of tumor cells depends on recognition between
77 phagocytic receptors on the macrophages and “eat me” signals on the tumor cell surface that enable
78 engulfment of the tumor cell by the macrophages [7, 8]. A crucial insight emerged from our previous
79 research, revealing that macrophages possess the capability to engulf ferroptotic cells through non-
80 canonical “eat-me” signals, which prime these cells for engulfment via Toll-like receptor 2 (TLR2) [6].
81 Despite this milestone, the exact mechanism by which phospholipid peroxidation within macrophages
82 impacts their phagocytic capabilities during ferroptosis-based tumor treatment remains elusive.
83 Therefore, understanding the relationship between phospholipid-peroxidized macrophages and
84 phagocytosis is paramount to realizing the potential of ferroptosis in cancer therapy.

85 In this study, we uncovered a hitherto unknown mechanism by which phospholipid peroxidation
86 in macrophages diminishes their ability to phagocytose ferroptotic tumor cells, ultimately fostering a
87 state of resistance to ferroptosis-based anticancer interventions. At the heart of this mechanistic
88 revelation lies the identification of oxygenated phosphatidylethanolamine (oxPEs), specifically SAPE-
89 OOH, which selectively competes with TLR2 binding, resulting in the inhibition of the translocation of
90 the TLR2/CNPY3 complex to the plasma membrane. Additionally, the TLR2 retained within the
91 endoplasmic reticulum (ER) initiates the recruitment of the E3 ligase MARCH6, triggering a
92 proteasome-dependent degradation pathway. Conclusively, this discovery sheds light on a novel
93 molecular mechanism underlying macrophage phospholipid peroxidation-induced tumor resistance to
94 ferroptosis therapy and underscores the TLR2-MARCH6 axis as a promising therapeutic target for
95 cancer treatment.

Results

Phospholipid peroxidation of macrophages evokes tumor resistance to ferroptosis therapy.

Currently, targeting the delivery of ferroptosis inducers (FIN) to the tumor microenvironment (TME) is a promising therapeutic strategy to enhance the efficacy of tumor therapy [9]. However, it also may cause phospholipids peroxidation in the TME, which limits its efficacy and applicability. In pursuit of a deeper understanding of the repercussions of phospholipid peroxidation within the TME during ferroptosis therapy, we firstly constructed a acidic TME targeted-delivery system for sulfasalazine (SSZ, FDA-approved drug applied for anti-tumor with class I FIN activity [10, 11]) by the modification of pH (low) insertion diblock copolymer (mPEG-PCL), named as mPEG-PCL-SSZ (Fig. S1a-e). E0771 cells were subcutaneously injected into C57BL/6J mice to establish mouse breast cancer model. Once the tumors reached a volume of 100 mm³, E0771-bearing mice were administered saline (WT) or mPEG-PCL-SSZ (equivalent to 40 mg SSZ kg⁻¹) every day for two consecutive weeks via intravenously route. As shown in Fig. 1a and 1b, mPEG-PCL-SSZ treatment exhibited an inhibition of tumor growth compared with the WT group. However, the treatment yielded a V-shaped curve displaying an initial inhibition of tumor growth, followed by a rapid increase (Fig. 1c). Immunofluorescence staining demonstrated a notable accumulation of the phospholipid peroxidation end product, 4-hydroxynonenal (4-HNE) in TME macrophages in the mPEG-PCL-SSZ treatment group (Fig. S2a). This was further verified by LC-MS/MS analysis, which identified the presence of oxidized phospholipids in the TME macrophages. Redox phospholipidomics analysis revealed distinct oxygenated phospholipid profiles in TME macrophages between WT and mPEG-PCL-SSZ groups (Fig. S2b and Fig. 1d-e). Among all classes of oxygenated phospholipids (oxPLs) detected, oxygenated phosphatidylethanolamines (oxPEs) were the most predominant species with significant increases in the TME macrophages in the mPEG-PCL-SSZ treatment group (Fig. 1f-g). Further analysis of singly, doubly, and triply oxidized phospholipids indicated that PE hydroperoxides were the primary form of oxPLs. Among these, SAPE-OOH (PE (38:4) + 2O) accounted for the highest increase in the mPEG-PCL-SSZ group (Fig. 1g-h). These results raised the possibility that phospholipid-peroxidation of TME macrophages may be responsible for tumor resistance to ferroptosis therapy.

Glutathione peroxidase 4 (GPX4) is a key cellular regulator of phospholipid peroxidation, and its conditional deletion is known to cause significant peroxidation of membrane phospholipids [12, 13]. To investigate the correlation between peroxidation of macrophages and resistance to therapy, *Gpx4*^{fl/fl} mice

were crossed with *Lyz2^{cre}* mice to obtain mice heterozygous for myeloid-specific *Gpx4* deficiency (called “*Gpx4^{CKO}* mice” hereafter) (Fig. S3a-b). Analysis of 4-HNE formation revealed that 4-HNE was significantly elevated in bone marrow derived macrophages (BMDMs) and TME macrophages obtained from *Gpx4^{CKO}* mice (Fig. S2a and Fig. S3b). Remarkably, tumors in *Gpx4^{CKO}* mice were nonresponsive to mPEG-PCL-SSZ, as evidenced by lack of substantial changes to tumor volumes and weights when compared to the untreated *Gpx4^{CKO}* group (Fig. 1i-l). Immunofluorescence staining revealed a significantly higher 4-HNE in TME macrophages in the *Gpx4^{CKO}* + mPEG-PCL-SSZ group as compared with the untreated *Gpx4^{CKO}* group (Fig. S2a), suggesting a role for peroxidized macrophages in conferring tumor resistance to ferroptosis therapy.

Further confirmation of a connection between phospholipid-peroxidation in TME macrophages and resistance to ferroptosis therapy was obtained using a breast cancer model. E0771 cells were subcutaneously injected into WT and *Gpx4^{CKO}* mice, followed by intratumoral administration of saline or (1S, 3R)-RSL3 (a selective GPX4 inhibitor, 100 mg/kg) twice a week for two consecutive weeks. As shown in Fig. S3C, the therapeutic period did not significantly affect the body weight of the animals. As expected, intratumorally administration of RSL3 led to inhibition of tumor growth, as evidenced by a reduction in tumor volume and tumor weight compared to the WT group (Fig. 1m-p). In sharp contrast, tumors in *Gpx4^{CKO}* mice were nonresponsive to RSL3 treatment, as evidenced by lack of substantial change in tumor volumes and tumor weights compared to the *Gpx4^{CKO}* group (Fig. 1m-p). Immunofluorescence staining revealed significant accumulation of 4-HNE in TME macrophages after RSL3 treatment (Fig. 1q). These results unequivocally establish a pivotal role of peroxidized macrophages in conferring resistance to ferroptosis therapy in tumors.

147

148 **Phospholipid peroxidation impairs macrophage phagocytic capability**

Phagocytosis plays an essential role in clearance of dead cells, particularly during cancer therapy [14, 15]. Therefore, impaired phagocytosis of tumor cells might be detrimental to ferroptosis therapy. To address this possibility, the impact of phospholipid peroxidation on phagocytic clearance of tumor cells by TME macrophages was assessed. Indeed, results from immunohistochemistry (IHC) and immunofluorescence staining demonstrated significantly higher infiltration of macrophages in tumors treated with mPEG-PCL-SSZ or RSL3 compared to the WT group (Fig. 2a-b and Fig. S4a). A higher

magnification image of the tissue sections revealed that ferroptotic tumor cells were engulfed by macrophages in the tumor tissue from mice treated with mPEG-PCL-SSZ or RSL3 (Fig. 2a-b and Fig. S4a). However, in *Gpx4*^{CKO} animals, peroxidized macrophages exhibited significantly lower efficiency of phagocytosis of ferroptotic tumor cells in the tumor tissues of the animals treated with mPEG-PCL-SSZ or RSL3 compared to WT animals (Fig. 2a-b and Fig. S4a), providing a plausible explanation for the resistance of tumors in *Gpx4*^{CKO} mice to ferroptosis therapy. To better understand the inhibitory effect of ferroptosis mediated phospholipid peroxidation on macrophage phagocytosis, we compared the effect of RSL3 and Staurosporine (STS), respectively, on clearance of ferroptotic and apoptotic cell by macrophages *in vivo* and *in vitro*. Results showed that both ferroptotic and apoptotic cells were effectively engulfed by BMDMs (Fig. S4b). By sharp comparison, a remarkable decrease was observed in the phagocytic clearance of tumor cells in RSL3-treated mice compared to STS-treated mice (Fig. S4d). This distinct difference between *in vivo* and *in vitro* further demonstrated the detrimental influence of phospholipid peroxidation on macrophage phagocytosis, which was also supported by the obviously accumulation of 4-HNE in TME macrophages in RSL3 treatment but not in STS treatment (Fig. S4c). Taken together, these results raise the possibility that tumor resistance to ferroptosis therapy is due to a diminished ability of the macrophages to phagocytosis as a result of peroxidation.

To further confirm the impact of phospholipid peroxidation on phagocytosis *in vitro*, we take advantages of various ferroptosis inducers and inhibitors (Fig. 2c). The treatment with RSL3 at doses ranging from 0-0.5 μ M (24 h) did not reduce viability in THP1-derived macrophages (Fig. S5a-b). However, treatment with RSL3 resulted in a time dependent increase in lipid peroxidation which peaked at 6 h and lasted up to 12 h (Fig. S5c-d). This increase in peroxidation following RSL3 treatment occurred with a significant reduction in GPX4 expression and elevated 4-HNE level (Fig. S5e). Importantly, THP1 macrophages incubated with RSL3 for 6 h showed considerably dose-dependent reductions in phagocytosis of ferroptotic HL60 cells (Fig. 2d and Fig. S6a-b). Moreover, we investigated whether lipid peroxidation inhibitors, including ferrostatin-1 (Fer-1), deferoxamine (DFO) and N-acetyl-l-cysteine (NAC), could reverse the inhibitory effects of GPX4 inactivation on phagocytosis. Pretreatment with these inhibitors were revealed to reduce the accumulation of lipid free radicals (Fig. S7a) and restore the phagocytosis of ferroptotic HL60 cells in RSL3-treated THP1 macrophages (Fig. 2e and Fig. S7b-c). Similar results were also obtained in another two tumor cell lines, L1210 cells (Fig.

2f-g and Fig. S8a-b) and E0771 cells (Fig. S8c). To further confirm a nexus between GPX4-deficiency and peroxidation induced impairment of macrophage phagocytosis, GPX4 expression was knocked down in THP1 macrophages using siRNA. As shown in Fig. 2h-i and Fig. S6c, a decrease in GPX4 expression level in THP1 macrophages coincided with a reduction in phagocytosis of ferroptotic HL60 cells. In line with these observations, *Gpx4*^{CKO} BMDMs presented a significant reduction of phagocytic ability of ferroptotic L1210 cells (Fig. 2j-k and Fig. S8d).

It is generally accepted that incorporation of polyunsaturated fatty acids (PUFAs) in phospholipid enhances their peroxidation [16]. Based on this knowledge, we treated THP1 macrophages with exogenous linoleic acid (LA) and an elevated level of oxidized lipids was detected in cells. In the meantime, LA incorporation suppressed phagocytosis of ferroptotic HL60 cells in a dose dependent manner (Fig. S9a and Fig. S9c), and evoked even lower phagocytic efficiency in the presence of RSL3 treatment (Fig. 2l and Fig. S9d), uncovering an inverse correlation between the degree of phospholipid oxidation and phagocytosis (Fig. S9b). Erastin is an inhibitor of the cystine-glutamate exchange antiporter system that reduces cellular uptake of the key substrate cysteine for glutathione synthesis [17], thereby causing excessive accumulation of phospholipid peroxides (Fig. 2c). Erastin treatment considerably decreased the phagocytosis of ferroptotic HL60 cells by THP1 macrophages in a dose-dependent manner, with no significant effect on macrophage viability (Fig. 2m and Fig. S10a-b). Collectively, the above findings from multiple models of phospholipid peroxidation guarantee that phospholipid peroxidation in macrophages leads to dampened phagocytosis of ferroptotic cells.

The macrophage TLR2 receptor is involved in lipid peroxidation-impaired phagocytosis of ferroptotic tumor cells

In our previous study, we identified TLR2 as a crucial player in the clearance of ferroptotic cells by macrophages [6]. To test the involvement of TLR2 in resistance to ferroptosis therapy, *Tlr2* KO mice were subcutaneously injected with E0771 breast cancer cells. Once the tumor volume reached ~100 mm³, the mice were intratumorally administrated with saline, or (1S, 3R)-RSL3 (100 mg/kg) twice each week for two consecutive weeks (Fig. 3a). Fig. S10c shows that there is no significant changes in body weight between groups during the therapeutic period. In the WT animals, RSL3 treatment resulted in reduced tumor volumes and weights (Fig. 3b-e). In contrast, tumors in *Tlr2* KO mice were

213 nonresponsive to RSL3 treatment (Fig. 3b-e). In the meantime, when compared to the WT + RSL3
214 group, the efficiency of macrophages in phagocytosing ferroptotic tumor cells was obviously down-
215 regulated in *Tlr2* KO + RSL3 group, explaining the resistance of tumor to ferroptosis therapy in *Tlr2*
216 KO mice, and the inhibitory pattern is similar to that of *Gpx4*^{CKO} mice (Fig. 3f-g). These results indicate
217 that tumor resistance to ferroptosis therapy is contributed by the *Tlr2* KO-disrupted phagocytosis of
218 macrophage to ferroptotic tumor cell.

219 To further understand the effect of phospholipid peroxidation on phagocytosis of ferroptotic cells
220 via TLR2, we investigated the impact of phospholipid peroxidation on phagocytic clearance of
221 ferroptotic cells by *Tlr2* KO macrophages *in vitro*. Assessment of phagocytosis revealed that RSL3-
222 mediated phospholipid peroxidation notably repressed phagocytosis and clearance of ferroptotic L1210
223 cells by WT BMDMs in a dose-dependent manner, whereas no apparent down-regulation of phagocytic
224 efficiency was observed in *Tlr2* KO macrophages treated with a series of RSL3 concentrations (Fig. 3h-
225 j). Collectively, these studies reveal that TLR2 is critically involved in phospholipid peroxidation-
226 provoked impairment of ferroptotic cell clearance by macrophages and tumor resistance to ferroptosis
227 therapy.

228

229 **Accumulation of oxPEs in ER disrupted TLR2 trafficking to plasma membrane by attenuating** 230 **the interaction between TLR2 and CNPY3**

231 Given the critical role of TLR2 in the impairment of ferroptotic cell clearance by macrophages induced
232 by phospholipid peroxidation, we sought to gain a deeper understanding of the exact regulatory
233 relationship between phospholipid peroxidation and TLR2. Surprisingly, no significant alteration of
234 total TLR2 gene and protein levels observed in THP1 macrophages treated with 0.5 μ M RSL3 for 6 h
235 (Fig. 4a-b). This raised the possibility that our observations on impairment of ferroptotic cell clearance
236 was not dependent on TLR2 per se, but rather a phospholipid peroxidation induced defect in
237 transportation of TLR2 to the macrophage cell surface, which is critical for phagocytosis to ensue. To
238 test this, we measured the distribution of TLR2 in the plasma membrane (PM) and cytoplasm (Cyt) of
239 RSL3-treated THP1-derived macrophages and found that the levels of TLR2 in the PM fraction
240 decreased remarkably, while in cytoplasmic TLR2 increased (Fig. 4c). This observation was further
241 confirmed in *Gpx4*^{CKO} BMDM macrophages, where GPX4 deficiency also resulted in reduced

242 membrane TLR2 abundance and increased cytoplasmic TLR2 level (Fig. S12a). Under normal
243 physiological conditions, TLR2 is synthesized and transported from the ER to the PM [18]. To explore
244 whether phospholipid peroxidation mediated retention of TLR2 in cytoplasmic components is
245 predominantly located in the ER, we quantified the ER localization of TLR2 through ultra-
246 centrifugation purification and found that RSL3 for 6 h treatment significantly enhanced the distribution
247 of TLR2 in the ER (Fig. 4d-e). We next employed immunofluorescence colocalization studies to
248 visualize this phenomenon and observed that RSL3 for 6 h treatment resulted in a reduction in co-
249 localization of TLR2 with the PM marker E-Cadherin, and an increase in TLR2 colocalized with the
250 ER membrane marker Calnexin (Fig. 4f-g).

251 We have previously reported that TLR2 binds to oxPEs [6]. A scaffold protein
252 phosphatidylethanolamine binding protein 1 (PEBP1), which is required to form the ALOX15/PEBP1
253 complex that specifically generate oxPEs (Fig. 4h) [19]. In view of the accumulation of oxPEs revealed
254 in the TME macrophages in ferroptosis inducer-treated tumors (Fig. 1g-h), we hypothesized that ER-
255 specific oxPEs accumulation plays a key role in disrupting the transport of TLR2 to the PM, thereby
256 impairing the TLR2 subcellular distribution. As expected, ER phospholipid peroxidation induced by
257 transfection of ER-targeted ALOX15/PEBP1 (Fig. S11a-c) notably decreased the colocalization of
258 TLR2 in the PM and remarkably increased the distribution of TLR2 in ER (Fig. 4i-j). These findings
259 indicate that accumulation of oxygenated PE in the ER disrupts the transportation of TLR2 from the ER
260 to the PM, resulting in a decrease in the distribution of TLR2 on the PM.

261 Proper folding of TLR2 requires the molecular chaperone GP96 and subsequent interaction with
262 CNPY3 for transportation of the TLR2/CNPY3 complex to the cell surface [20, 21]. Conditional *Cnpy3*
263 deletion has been shown to impair subcellular distribution of TLR2 in the PM [22]. In order to clearly
264 investigate the potential mechanism of phospholipid peroxidation controlling TLR2 translocation, we
265 firstly determined the effect of phospholipid peroxidation on the expression of genes associated with
266 TLR2 translocation in THP1 macrophages. Nevertheless, no substantial effects on *GP96* and *CNPY3*
267 gene levels were observed in THP1 macrophages treated with 0.5 μ M RSL3 for 6 h (Fig. S12b).
268 Similarly, no significant changes to CNPY3 protein levels were observed (Fig. S12c). We further tested
269 whether phospholipid peroxidation impairs the interaction between TLR2 and CNPY3. As shown in Fig.
270 4j, RSL3 treatment for 6 h reduced the interaction between TLR2 and CNPY3, while Fer-1 pretreatment

reversed this inhibitory effect (Fig. 4k). Interestingly, RSL3 has no effect on TLR4 transport to the PM (Fig. S12d), which is also mediated by CNPY3 [23]. These data implicate a selective role for TLR2, wherein accumulation of oxPEs in the ER selectively competes with TLR2 binding, resulting in reduced transport of the TLR2/CNPY3 complex to the PM (Fig. 4l).

OxPEs in ER as a critical player mediates proteasome-dependent degradation of TLR2

The ER is central to synthesis, folding and transport of secretory and transmembrane proteins [24, 25]. Misfolded and improperly transported proteins are degraded via a proteasome-mediated process known as ER-associated degradation (ERAD) [26, 27]. Given this, we hypothesized that TLR2 transport failure may initiate proteasome-dependent degradation. To test this prediction, we examined TLR2 gene and protein levels at different time points during RSL3 treatment. As shown in Fig. 5a and Fig. 5b, no significant alteration of TLR2 gene level was observed at all time points, but TLR2 protein level was significantly reduced after 24 and 48 h of treatment with 0.5 μ M RSL3 in THP1 macrophages. Similar results were obtained in BDMD macrophages with GPX4 deficiency-induced phospholipid peroxidation (Fig. 5c). Using protein synthesis inhibitor cycloheximide (CHX), we further demonstrated that RSL3-induced phospholipid peroxidation accelerated TLR2 degradation in THP1 macrophages (Fig. 5d). Meanwhile, the treatment of MG132, a proteasome inhibitor, remarkably rescued RSL3-induced decrease of TLR2 in THP1 macrophages, whereas treatment with the autophagy inhibitor 3-MA did not (Fig. 5e). These results prompted us to speculate whether phospholipid peroxidation initiated proteasome-dependent degradation of TLR2. To test this hypothesis, TLR2 was immunoprecipitated to examine its ubiquitination level in THP1 macrophages in response to phospholipid peroxidation. Results revealed that RSL3 treatment for 48 h enhanced polyubiquitination of TLR2 (Fig. 5f). Subsequently, targeted generation of oxPEs in ER was established by co-transfection of ER-targeted ALOX15/PEBP1 and found that this condition also dramatically increased polyubiquitination level of TLR2 (Fig. 5g-h), and decreased phagocytosis of ferroptotic HL60 cells by THP1 macrophages (Fig. 5i and Fig. S13a). Collectively, these results suggest that the proteasome dependent degradation of TLR2, facilitated by accumulation of oxPEs in the ER, attenuates phagocytosis of ferroptotic cells.

To identify the E3 ligase responsible for TLR2 ubiquitination during phospholipid peroxidation,

we initially used the UbiBrowser database to make a prediction and MARCH6 was identified as a potential E3 ligase with the highest score and resident in the ER. Data from co-immunoprecipitation demonstrated that transfection of ER-targeted ALOX15/PEBP1 enhanced the interaction between TLR2 and MARCH6 (Fig. 6a). These observations prompted us to determine whether MARCH6 played an indispensable role in TLR2 ubiquitination. In this regard, we determined that knockdown of MARCH6 by siRNA notably hindered ER-ALOX15/PEBP1-mediated TLR2 protein decline (Fig. 6b-c). Furthermore, depletion of MARCH6 dramatically decreased the ubiquitination level of TLR2 (Fig. 6d). Gain-of-function experiments in HEK293 cells demonstrated that MARCH6 overexpression exacerbated ER-targeted ALOX15/PEBP1-induced decrease of TLR2 protein level, coinciding with increased ubiquitination of TLR2 (Fig. 6e-f and Fig. S13b). Taken together, these data indicate that ER oxPEs recruits E3 ligase MARCH6 to initiate the ubiquitination process of TLR2, thus impeding macrophage phagocytosis of ferroptotic cells.

312

Identification of SAPE-OOH acts as the executioner that mediates ubiquitin degradation of TLR2

To identify the key executioners involved in ubiquitin degradation of TLR2, purified ER membranes were extracted for LC-MS/MS analysis to detect oxygenated products. We determined that transfection of ER-targeted ALOX15/PEBP1 led to the appearance of oxPLs across all species (Fig. 7a). Orthogonal partial least squares discriminant analysis (OPLS-DA), a multivariate analysis method for the regression modeling of multiple dependent variables to multiple independent variables [28], identified a distinct difference in oxPLs from ER between Vector and ALOX15/PEBP1 overexpression groups (Fig. 7b). Among all classes of oxPLs, oxPEs were the most predominant species with significant fold difference (Fig. 7c-d), and SAPE-OOH (PE (38:4) + 2O) exhibited the most significant increase in the ALOX15/PEBP1 transfected cells (Fig. 7e-f and Fig. S13c). These results suggest that PE hydroperoxides, particularly, SAPE-OOH, prevailed substantially in the ER, raising the possibility of this species potentially mediating TLR2 ubiquitination. This possibility was confirmed by the observation that exogenous SAPE-OOH added to THP1 macrophages caused ubiquitination of TLR2 (Fig. 7g). Moreover, SAPE-OOH enriched THP1 macrophages showed a reduced ability to phagocytose ferroptotic HL60 cells (Fig. 7h and Fig. S13d). Thus, these experiments together provide a direct evidence proving the causal relationship between ferroptosis-induced ER SAPE-OOH accumulation

and the instability of TLR2, which disrupts its translocation to PM and thus impairs macrophage clearance of ferroptotic tumor cells.

TLR2 agonist enhances antitumor efficacy of ferroptosis inducer.

The above findings implies that inhibiting accumulation of phospholipid peroxides or maintaining TLR2 protein level is expected to recover macrophage phagocytosis and enhance the anti-tumor efficiency of ferroptosis inducers. However, phospholipid peroxidation inhibitors are not macrophage-specific and may mitigate the killing effect of ferroptosis inducers on tumor cells. Thus, augmenting TLR2 expression in macrophages holds promise as a synergistic approach to enhance the efficacy of ferroptosis inducers in tumor treatment. Our previous research have highlighted the favorable performance of the TLR2 agonist SMU-Z1 in boosting TLR2 protein expression in macrophages [6]. To assess the therapeutic efficacy of combining SMU-Z1 with ferroptosis inducers, a mixture of E0771 cells and SMU-Z1-pretreated *Gpx4*^{CKO} BMDMs was subcutaneously injected into C57BL/6J mice at a ratio of 5:1. When the tumor volume reached about 100 mm³, mice were intratumorally injected with saline or 50 mg/kg (1S, 3R)-RSL3 twice each week for two consecutive weeks (Fig. 8a). Throughout the therapeutic period shown in Fig. S13e, no significant changes were observed in the body weight of the mice. Consistent with our hypothesis, it is noteworthy that tumor growth in the SMU-Z1 and RSL3 groups slowed down, as depicted by reduced tumor volume and tumor weight as compared to the WT group (Fig. 8b-e). Furthermore, the combination of SMU-Z1 with RSL3 exhibited an even greater reduction in tumor volume and tumor weight (Fig. 8b-e). These findings strongly indicate that SMU-Z1 enhances the antitumor efficacy of ferroptosis inducers. We also observed a significant increase in the phagocytic clearance of ferroptotic tumor cells by macrophages in the tumor tissues of the SMU-Z1 + RSL3 group compared to the RSL3 group, which was accompanied by upregulation of TLR2 protein expression (Fig. 8f-g). Consistent with the stimulatory effect of SMU-Z1 *in vivo*, treatment with this agent also remarkably enhanced the phagocytosis of ferroptotic HL60 cells by THP1 macrophages (Fig. 8h and y Fig. S13f). These findings robustly support the notion that SMU-Z1 promotes phagocytosis of ferroptotic tumor cells by increasing TLR2 protein expression, thus enhancing the therapeutic effect of ferroptosis inducer. Collectively, our data suggest that the combination of SMU-Z1 and ferroptosis inducer represents a promising anti-tumor therapeutic strategy.

Discussion

Ferroptosis, a form of regulated nonapoptotic cell death that is characterized by iron-dependent accumulation of phospholipid peroxidation products, has been touted to have extraordinary potential in cancer therapy. However, ferroptosis inducers are not cell-specific, which currently limits its success as a therapeutic modality. Macrophages, as the predominant immune cell population in the TME, play a vital role in recognizing and phagocytosing ferroptotic tumor cells and is crucial for tumor immunosurveillance [5, 6]. Recent studies have suggested that lipid accumulation, driven by the scavenger receptor CD36 in TME macrophages, plays a crucial role in tumor development and progression [29, 30]. Nonetheless, the precise mechanism(s) of how phospholipid peroxidation in the TME could influence phagocytosis of ferroptotic tumors by macrophages remains unclear. Unraveling the relationship between phospholipid-peroxidized macrophages and phagocytosis holds immense potential for advancing ferroptosis-based cancer therapy. In this study, we revealed that phospholipid peroxidation in macrophages dampened its phagocytic proficiency for ferroptotic tumor cells and evoked tumor resistance to ferroptosis therapy. We used a diverse combination of approaches including *Gpx4* deficient mice, esterified oxygenated PUFA, and lipid peroxidation inhibitors to arrive at our conclusions. Collectively, these observations establish an innovative concept that tumor resistance to ferroptosis therapy is due to dampening of phagocytosis in phospholipid peroxidized macrophages.

Phagocytosis is dependent on the mutual recognition between phagocytic receptors on the surface of phagocytes and unique “eat me” signal on the target cell (e.g. tumor cell) surface [7, 31]. In a previous study, we identified TLR2 as a key player in the recognition and clearance of ferroptotic tumor cells [6]. The present findings further support the critical involvement of TLR2 in phospholipid peroxidation-provoked impairment of ferroptotic cell clearance by macrophages. We determined that these results were not due to alterations in TLR2 at the gene or protein level, but due to the appearance of oxygenated PE species in the ER, which negatively impacted formation of the TLR2/CNPY3, a critical step for ensuring that TLR2 is delivered to the PM surface.

The ER is a pivotal organelle involved in protein folding and assembly, particularly for transmembrane and secretory proteins [24]. Misfolded proteins, or otherwise improperly transport proteins are directed to ERAD machinery, which recognizes and targets them for proteasomal degradation [32, 33]. We show here that GPX4 inactivation, or GPX4 deficiency-induced phospholipid

peroxidation results in accumulation of oxygenated PE in the ER, and promoted ubiquitin directed degradation of TLR2. In attempting to understand the link between phospholipid peroxidation and TLR2 ubiquitination, we have identified MARCH6 as the E3 ligase responsible for TLR2 ubiquitination during phospholipid peroxidation. Notably, TLR2 interacts with MARCH6, and this interaction is substantially enhanced by the accumulation of oxygenated PE in the ER. Furthermore, depletion of MARCH6 through siRNA abolished the stimulatory effect of oxygenated PE on ubiquitination of TLR2, whereas overexpression of MARCH6 increases TLR2 ubiquitination. By employing phospholipidomics analysis of ER lipids, we have identified SAPE-OOH acts as the key executioner that mediates ubiquitin degradation of TLR2, an effect that could be reproduced using exogenous SAPE-OOH. In light of these findings, inhibiting the accumulation of phospholipid peroxides, or promoting the expression of TLR2 protein may alleviate macrophage phagocytic inhibition enhance the therapeutic efficacy of ferroptosis inducers for tumor treatment. Our results strongly support the notion that the TLR2 agonist SMU-Z1 enhances efficiency of phagocytosis and clearance of ferroptotic tumor cells by increasing TLR2 protein expression, thereby synergizing with the ferroptosis inducer to further inhibit tumor growth.

In summary, our study presents a novel concept that tumor resistance to ferroptosis therapy is caused by phospholipid peroxidation, which impairs macrophage phagocytosis of ferroptotic tumor cells. Through our mechanistic investigation, we have identified SAPE-OOH as the primary mediator responsible for the reduced subcellular localization of TLR2 on macrophages, leading to impaired transport of the TLR2/CNPY3 complex to the PM. Additionally, TLR2 retention in the ER triggers proteasome-dependent ubiquitin degradation by recruiting the E3 ligase MARCH6, which further hinders macrophage phagocytosis and clearance of ferroptotic tumor cells.

408

409 **Materials and methods**

410 **Preparation of SSZ-loaded micelles**

411 The nanoprecipitation method was used to prepare SSZ micelles. The mPEG-PCL copolymer (150 mg)
412 and SSZ (100 mg) were dissolved in 20 mL of acetone and sonicated for 30 min. Then, the mixture was
413 gently injected dropwise into 60 mL of deionized water under stirring at 300 rpm. The mixture was
414 stirred magnetically at room temperature for 48 h to allow complete evaporation of acetone and self-
415 assembly of the amphiphilic copolymer and hydrophobic drug to form micelles. The resulting yellow

dispersion was filtered through a 0.45 µm filter, and the mPEG-PCL-SSZ micelles were obtained by centrifugation at 13,000 rpm for 20 min. The final dried form of mPEG-PCL-SSZ micelles was obtained after freeze-drying at 14 Pa pressure and -58°C. For *in vivo* imaging, DIR dyes are encapsulated in copolymer micelles by the same method as above.

Characterization of the micelles

The microstructure of the micelles was observed with a transmission electron microscopy (TEM) instrument (JEM, 1400 Flash). The zeta potential and size distribution of the micelles were analyzed by dynamic light scattering using a zeta sizer instrument (Nano ZS, Malvern Instruments Co., UK).

Drug loading and encapsulation efficiency calculation

The drug loading (%) was calculated from the weight of unencapsulated SSZ in the supernatant and the freeze-dried form of the micelles.

$$\text{Drug loading (\%)} = \frac{\text{Weight}_{\text{unencapsulated}}}{\text{Weight}_{\text{final dried form micelles}}}$$

Drug encapsulation efficiency (%EE) was determined based on the unencapsulated SSZ in the supernatant and the initial input amount of SSZ.

$$\text{Encapsulation efficiency (\%)} = \frac{\text{weight}_{\text{unencapsulated}}}{\text{Weight}_{\text{initial input}}}$$

The concentration of SSZ in the supernatant was calculated from the standard curve of the drug by measuring the absorbance at 359 nm using a microplate reader (Elx800, BioTek, USA).

In vitro release of SSZ

The SSZ loaded micelles was dispersed in 10 mL of PBS at different pH (pH 5.5, pH 6.5, or pH 7.4) and shaken at 100 rpm in a constant temperature shaker at 37°C. At specific time points, 1 mL of the dispersion was centrifuged at 13000 rpm for 10 min and 100 µL of the supernatant was taken to determine the absorbance at 359 nm. The concentration of released SSZ was used to estimate the percentage of cumulative drug release (%):

$$\text{Cumulative drug release (\%)} = \frac{V_t \sum_{i=1}^{n-1} C_i + V_0 C_n}{\text{Weight}_{\text{SSZ}}}$$

where $\text{Weight}_{\text{SSZ}}$ is the amount of SSZ in the micelles, V_0 is the total volume of the release system ($V_0 = 10$ mL), V_t is the volume of the replaced media ($V_t = 1$ mL), and C_n is the concentration of SSZ in the release system.

Animals and treatment

Tlr2 KO C57BL/6J mice (Stock No.: 004650), *Gpx4*^{fl^{ox}/fl^{ox}} C57BL/6J mice (Stock No.: 027964) and *Lyz2*^{cre} C57BL/6J mice (Stock No.: 004781) were maintained at a constant temperature (22 ± 2°C), humidity (55 ± 5%), and illumination (12 h light/dark cycle). Mice were adaptive feed for a week before experiment.

To investigate the role of macrophage phospholipid peroxidation in tumor growth, *Gpx4*^{fl/fl} C57BL/6J mice were crossed with *Lyz2*^{cre} C57BL/6J mice to construct mice that were heterozygous for myeloid-specific *Gpx4* deficiency (*Gpx4*^{CKO} C57BL/6J mice). Wild type (WT) or *Gpx4*^{CKO} C57BL/6J mice (female, 8-week-old) were randomly divided into four groups: WT, *Gpx4*^{CKO}, mPEG-PCL-SSZ, *Gpx4*^{CKO} + mPEG-PCL-SSZ. Mice were subcutaneously injected with E0771 cells (2 × 10⁶ cell/0.2 mL) to establish breast cancer model. Mice were intratumorally administrated with saline (WT), mPEG-PCL-SSZ (40 mg SSZ equiv kg⁻¹) twice each week for two consecutive weeks upon the tumor volume reaching to 100 mm³.

To further determine whether phospholipid-peroxidized macrophages and therapeutic resistance were commonly correlated in various ferroptosis inducer. WT or *Gpx4*^{CKO} C57BL/6J mice were randomly divided into four groups: WT, *Gpx4*^{CKO}, RSL3, *Gpx4*^{CKO} + RSL3. Mice were subcutaneously injected with E0771 cells (2 × 10⁶ cell/0.2 mL) to establish breast cancer model. Mice were intravenously administrated with saline (WT), 100 mg/kg (1S, 3R)-RSL3 every day for two consecutive weeks upon the tumor volume reaching to 100 mm³.

Tlr2 KO mice were utilized to verify the role of TLR2 on tumor ferroptosis treatment resistance. WT or *Tlr2* KO C57BL/6J mice (female, 8-week-old) were randomly allocated into four groups: WT, *Tlr2* KO, WT + RSL3, *Tlr2* KO + RSL3. Mice were inoculated with E0771 cells (2 × 10⁶ cell/0.2 mL) to establish breast cancer model. Mice were intratumorally administrated with saline or 100 mg/kg (1S, 3R)-RSL3 twice each week for two consecutive weeks upon the tumor volume reaching to 100 mm³ (Fig. 3A).

To investigate the therapeutic efficiency of TLR2 agonist combined with ferroptosis inducers, E0771 cells were mixed with or without TLR2 agonist SMU-Z1-pretreated *Gpx4*^{CKO} BMDM macrophages at a ratio of 5:1 and then injected subcutaneously into C57BL/6J mice. Mice were intratumorally injected with saline or 50 mg/kg (1S, 3R)-RSL3 twice each week for two consecutive weeks when the tumor volume reaching to 100 mm³.

The body weight of the E0771-bearing mice was tracked every day. Tumor volume of each mouse was measured every three days and calculated according to the following equation: tumor volume (mm³) = [tumor length (mm)] × [tumor width (mm)]/2. Mice were euthanatized and the tumor tissues were weighted, fixed in 4% paraformaldehyde at the end of administration.

Cell culture and treatment

HL60 cells were maintained in RPMI medium 1640 (ThermoFisher Scientific, USA). L1210 cells, HEK293 cells and E0771 cells were maintained in DMEM (ThermoFisher Scientific, USA), supplemented with 10% fetal bovine serum (PAN biotech, Germany). Human monocytic cell line (THP1 cells) was cultured in RPMI medium 1640 supplemented with 10% fetal bovine serum, 2 mM β -mercaptoethanol and 50 mM glutamine. THP-1 cells were differentiated into macrophages by PMA (0.2 μ M) exposure for 72 h.

The isolation and purification of bone marrow-derived macrophages (BMDMs) were performed according to the reported protocol [34]. 6-8 weeks old WT, *Tlr2* KO or *Gpx4*^{CKO} C57BL/6J mice were anesthetized and two femurs were obtained in sterile PBS. The bone marrow cavity of femurs was flushed by sterile PBS and passing through Falcon Cell Strainer (0.4 μ m, BD Biosciences, USA). Murine BMDMs were harvested by centrifugation at 1000 × g for 8 min and differentiated in DMEM/F12 containing M-CSF exposure (100 ng/mL) for 7 days, and identified by flow cytometry. Macrophages were stimulated and differentiated into M1-like macrophages by LPS (100 ng/ml) and IFN γ (20 ng/ml) exposure for 24 h. Macrophages were stimulated and differentiated into M2-like macrophages by IL-4 (25 ng/ml) exposure for 24 h. All cells were cultured in medium containing 10% fetal bovine serum and maintained in incubators containing 5% CO₂ at 37°C, and 95% humidity.

Macrophage staining and cell sorting

Resected tumors were mechanically dissociated with scissors and digested in 5 ml PBS containing 10 μ g/ml Liberase for 30 min at 37 °C. The solution was filtered through a 0.45 μ m filter and centrifuged for 5 min at 300g before resuspension in FACS buffer. For macrophage sorting experiments, single cell suspensions were stained in 100 μ l PBS containing 0.25 μ g of each antibody against F4/80 and CD11b, and sorted on a FACS Aria II benchtop cell sorter (Becton Dickinson).

Immunohistochemistry analysis

The tumor tissues were fixed with 4% paraformaldehyde and embedded in paraffin. To assess

macrophage phagocytosis in tumor tissues, tumor tissues cut into 4 μ m slices and processed according to standard deparaffinization and rehydration methods. The tumor slices were incubated with rat anti-F4/80 (1:100) overnight at 4 $^{\circ}$ C, followed by labeling with HRP-conjugated secondary antibodies and visualized by DAB Detection Kit. Slices were stained with hematoxylin and imaged by a Digital Microscope and Scanner (M8, Precipoint GmbH, Germany).

Immunofluorescence analysis

Cells of each group were fixed in 4% paraformaldehyde for 10 min, followed by permeabilizing with Triton-X100 (0.1%) for 10 min in the cell immunofluorescence analysis. After blocking with 20% goat serum for 30 min, they were incubated with goat anti-TLR2 (1:100), rabbit anti-Cadherin (1:100) or rabbit anti-Calnexin (1:100) overnight at 4 $^{\circ}$ C. The secondary antibodies conjugated with Alexa Fluor 488 donkey anti-goat IgG (H+L) and 555 goat anti-rabbit IgG (H+L) in a dilution of 1:200 for 2 h at 37 $^{\circ}$ C. Nuclei were stained with DAPI in a dilution of 1:1000 for 10 min, and cells were imaged using a ZEISS LSM 880 confocal laser scanning microscope (Carl Zeiss AG, Oberkochen, Germany).

Tumor tissues were performed to a frozen section and cut into 10 μ m slices in the tissue immunofluorescence analysis. Tumor tissue slices were fixed in 4% paraformaldehyde for 10 min. After blocking with 20% goat serum for 30 min, they were incubated with rat anti-F4/80 (1:100), rabbit anti-4-HNE (1:100) or rabbit anti-iNOS (1:100) overnight at 4 $^{\circ}$ C. The secondary antibodies conjugated with Alexa Fluor 488 goat anti-rabbit IgG (H+L) and 555 goat anti-rabbit IgG (H+L) in a dilution of 1:200 for 2 h at 37 $^{\circ}$ C. Nuclei were stained with DAPI in a dilution of 1:1000 for 10 min, and cells were imaged using a ZEISS LSM 880 confocal laser scanning microscope.

Assessment of cell viability

Cells were dispensed in a 96-well plate at a density of 5×10^3 cells. Cells were incubated with RSL3 or Erastin for indicated periods of time, followed by processed Cell counting kit-8 according to the manufacturer's instructions. The absorbance was measured at 490 nm by microplate reader (Thermo Fisher Scientific, Waltham, MA, USA).

PI staining

Cells were dispensed in a 6-well plate at a density of 5×10^5 cells. Cells were incubated with RSL3 for indicated time, followed by staining with 0.05 mg/mL propidium iodide (PI) for 30 min at 4 $^{\circ}$ C and then

collected for analysis by a Beckman Coulter's CytoFLEX flow cytometer (Beckman Coulter, Inc., California, USA).

Assessment of phospholipid peroxidation

Cells were dispensed in a 6-well plate at a density of 5×10^5 cells. Cells were treated with RSL3 (0.5 μ M) for different time periods (0, 3, 6, 12 and 24 h) or transfected with pcDNA3.1-ER-PEBP1-HA and pcDNA3.1-ER-ALOX15-Flag for 48 h. After treatment, cells were incubated with C11-BODIPY^{581/591} (1 μ M) or Liperfluo (10 μ M) for 30 min. Then, the cells were collected and assessed for the phospholipid peroxidation by a Beckman Coulter's CytoFLEX flow cytometer, or imaged by a ZEISS LSM 880 confocal laser scanning microscope.

Determination of phagocytosis *in vitro*

HL60, L1210 or E0771 cells were pretreated with RSL3 for 6 h (ferroptotic cells) and labeled with CMFDA (1 μ M) for 30 min. THP1 macrophages were treated with RSL3 (0.5 μ M) for 6 h and incubated with CD11b (0.5 μ g/mL) for 30 min (for flow cytometry) or CellTracker Red CMTPX (1 μ M) for 30 min (for confocal microscopy). BMDMs were incubated with F4/80 (0.5 μ g/mL) for 30 min. HL60, L1210 or E0771 cells were collected and co-cultured with macrophages (THP1 macrophages or BMDMs). And the ratio of macrophages and ferroptotic tumor cells is 1 to 10. Afterward, unengulfed HL60, L1210 or E0771 cells were removed and the macrophages were collected for analysis by a Beckman Coulter's CytoFLEX flow cytometer equipped with FlowJo X 10.0.7 R2, or imaged by a ZEISS LSM 880 confocal laser scanning microscope.

qPCR analysis

Total RNA from cells was extracted by Trizol reagent. RNA was quantified and converted into cDNA by TranScript One-Step gDNA Removal and cDNA Synthesis Kit according to the manufacturer's instructions. qPCR was performed by TransStart Top Green qPCR SuperMix Kit and analyzed by CFX Connect Real-Time PCR Detection System (Bio-Rad Laboratories, CA, USA). The samples of each group were normalized by subtracting the threshold cycle value of GAPDH. The primer sequences are listed in the Supporting Information Table S2.

Western bolt analysis

Cells or tumor tissues were resuspended in RIPA lysis buffer and total proteins were isolated. The supernatants were obtained after centrifugation at $12,000 \times g$ for 10 min and quantified by Pierce BCA

Protein Assay Kit. Briefly, protein samples were separated in 8-12% gradient SDS-PAGE gels on and transferred into PVDF membrane (0.45 μ m, Millipore). The membranes were blocked with 5% non-fat milk diluted in TBST buffer for 1.5 h. and incubated with primary antibodies followed by HRP-conjugated anti-rabbit, anti-goat or anti-mouse secondary antibodies. The protein expressions were visually assessed by FDbio-Pico ECL Kit (FD8000, Fude Biological Technology) and imaged by Tanon 5200 Chemiluminescent Imaging System (Tanon, Shanghai, China).

siRNA/plasmids transfection

The siRNA targeting *GPX4* and *MARCHF6* (RiboBio) were transfected to HEK293 cells and THP1 macrophages, and a non-targeting siRNA was used as negative control. Lipofectamine™ 2000 and siRNA were diluted in Opti-MEM media (Life Technologies) at a concentration of 50 nM. Cells were incubated with the Opti-MEM-siRNA mixture for 6 h and cultured in fresh full media for 42 h. The sequences of siRNA were described in Supplementary Methods Table S3. Plasmids including pcDNA3.1-PEBP1-HA, pcDNA3.1-ALOX15-Flag, pcDNA3.1-TLR2-Myc and pcDNA3.1-MARCH6-His were transfected to HEK293 cells and THP1 macrophages cells using Neofect™ DNA transfection reagent.

Purification and validation of plasma membrane and cytoplasm

The plasma membrane and cytoplasm of THP1 macrophages/HEK293 cells (5×10^7 cells) were isolated by Minute Plasma Membrane Protein Isolation Kit according to manufacturer's instructions. The obtained plasma membrane and cytoplasm preparations (including cytosol fraction and organelles) were identified by western blot analysis by antibodies against markers of various biofilms, including plasma membrane (cadherin), endoplasmic reticulum (calnexin), cytoplasm (β -actin), mitochondria (VDAC), as well as Golgi apparatus (GM130).

ER purification

THP1 macrophages/HEK293 cells (5×10^8 cells) were mixed with the hypotonic extraction buffer (10 mM HEPES, 0.25 M sucrose, 25 mM potassium chloride and 1 mM EGTA) for 1 h at 4 °C. Subsequently, the cells were collected after centrifugation at $740 \times g$ for 10 min and suspended in the isotonic extraction buffer (1 mM EGTA, 10 mM HEPES, and 25 mM potassium chloride). Then the cells were transferred to a Dounce homogenizer and broken with the Dounce homogenizer. The homogenization buffer was centrifuged at $1000 \times g$ for 15 min. The supernatant fraction was centrifuged

at 9000 × *g* for 15 min at 4 °C. The obtained isotonic extraction buffer was centrifuged at 100,000 × *g* in an ultracentrifuge for 60 min at 4 °C. Finally, the endoplasmic reticulum fractions were collected and identified by western blot analysis by antibodies against markers of various biofilms, including plasma membrane (cadherin), endoplasmic reticulum (calnexin), cytoplasm (β -actin), mitochondria (VDAC), as well as Golgi apparatus (GM130).

LC–MS/MS-based phospholipidomics analysis

MS and MS/MS analysis of PLs was performed on a Q-exactive hybrid-quadrupole-orbitrap mass spectrometer (Thermo Fisher Scientific). Analysis was performed in negative ion mode at a resolution of 70000 for the full MS scan and 17,500 for the MS2 scan in data-dependent mode. The scan range for MS analysis was 400-1,800 *m/z* with a maximum injection time of 200 ms using microscan. A maximum injection time of 500 ms was used for high-energy collisional dissociation (HCD-MS2) analysis with collision energy set to 24 with an inclusion list for phospholipids including PE, PC, PS, PI and their oxidized and deuterated products. The isolation window of 1.0 Da was set for the MS and MS2 scans. Capillary spray voltage was set at 2.8 kV, and capillary temperature was 320 °C. The S-lens Rf level was set to 60.

Co-IP analysis

Cell samples (THP1 macrophages or HEK293 cells) were harvested and lysed with RIPA buffer containing protease inhibitor for Co-IP assays. Equivalent amount of protein was incubated with anti-MAVS, anti-TLR2, anti-CNPY3, anti-Myc, or anti-His antibody and Protein A/G Agarose. The IP complexes were collected and washed five times with lysis buffer after immunoprecipitation. The immunoprecipitates were separated in 8–12% gradient SDS-PAGE gels and analyzed by western blotting.

Statistical analysis

All data were represented as mean ± standard deviation (SD) and analyzed by IBM SPSS Statistics 25. *P* values were determined using independent samples *t*-test, one-way ANOVA with LSD post hoc test or two-way repeated measures ANOVA. *P* < 0.05 is considered statistically significant.

Data availability

Data are available upon reasonable request.

617 **References**

- 618 [1] Zhang C, Liu X, Jin S, Chen Y, Guo R. Ferroptosis in cancer therapy: a novel approach to reversing
619 drug resistance. *Mol Ther.* 2022;21:47.
- 620 [2] Wang H, Cheng Y, Mao C, Liu S, Xiao D, Huang J, et al. Emerging mechanisms and targeted therapy
621 of ferroptosis in cancer. *Mol Ther.* 2021;29:2185-208.
- 622 [3] Cassetta L, Pollard J W. Targeting macrophages: therapeutic approaches in cancer. *Nat Rev Drug*
623 *Discov.* 2018;17:887-904.
- 624 [4] McCracken M N, Cha A C, Weissman I L. Molecular pathways: activating T cells after cancer cell
625 phagocytosis from blockade of CD47 “Don't Eat Me” signals. *Clin Cancer Res.* 2015;21:3597-601.
- 626 [5] Liang C, Zhang X, Yang M, Dong X. Recent progress in ferroptosis inducers for cancer therapy.
627 *Adv Mater.* 2019;31:1904197.
- 628 [6] Luo X, Gong H-B, Gao H-Y, Wu Y-P, Sun W-Y, Li Z-Q, et al. Oxygenated phosphatidylethanolamine
629 navigates phagocytosis of ferroptotic cells by interacting with TLR2. *Cell Death Differ.* 2021;28:1971-
630 89.
- 631 [7] Lecoultre M, Dutoit V, Walker P R. Phagocytic function of tumor-associated macrophages as a key
632 determinant of tumor progression control: a review. *J Immunother Cancer.* 2020;8.
- 633 [8] Boada-Romero E, Martinez J, Heckmann B L, Green D R. The clearance of dead cells by
634 efferocytosis. *Nat Rev Mol Cell Biol.* 2020;21:398-414.
- 635 [9] Xue C-C, Li M-H, Zhao Y, Zhou J, Hu Y, Cai K-Y, et al. Tumor microenvironment-activatable Fe-
636 doxorubicin preloaded amorphous CaCO₃ nanoformulation triggers ferroptosis in target tumor cells.
637 *Sci Adv.* 2020;6:eaax1346.
- 638 [10] Chen X, Kang R, Kroemer G, Tang D. Broadening horizons: the role of ferroptosis in cancer. *Nat*
639 *rev Cancer clin oncol.* 2021;18:280-96.
- 640 [11] Yu H, Yang C, Jian L, Guo S, Chen R, Li K, et al. Sulfasalazine-induced ferroptosis in breast cancer
641 cells is reduced by the inhibitory effect of estrogen receptor on the transferrin receptor. *Oncol Rep.*
642 2019;42:826-38.
- 643 [12] Yang W S, SriRamaratnam R, Welsch M E, Shimada K, Skouta R, Viswanathan V S, et al.
644 Regulation of ferroptotic cancer cell death by GPX4. *Cell.* 2014;156:317-31.
- 645 [13] Seibt T M, Proneth B, Conrad M. Role of GPX4 in ferroptosis and its pharmacological implication.

Free Radic Biol Med. 2019;133:144-52.

[14] Li J, Ye Y, Liu Z, Zhang G, Dai H, Li J, et al. Macrophage mitochondrial fission improves cancer cell phagocytosis induced by therapeutic antibodies and is impaired by glutamine competition. *Nature cancer*. 2022;3:453-70.

[15] Duan Z, Luo Y. Targeting macrophages in cancer immunotherapy. *Signal transduction and targeted therapy*. 2021;6:127.

[16] Gan B. ACSL4, PUFA, and ferroptosis: new arsenal in anti-tumor immunity. *Signal Transduct Target Ther*. 2022;7:1-3.

[17] Li J, Cao F, Yin H-l, Huang Z-j, Lin Z-t, Mao N, et al. Ferroptosis: past, present and future. *Cell Death Dis*. 2020;11:1-13.

[18] Lee C C, Avalos A M, Ploegh H L. Accessory molecules for Toll-like receptors and their function. *Nat Rev Immunol*. 2012;12:168-79.

[19] Wenzel S E, Tyurina Y Y, Zhao J, Croix C M S, Dar H H, Mao G, et al. PEBP1 warden ferroptosis by enabling lipoxygenase generation of lipid death signals. *Cell*. 2017;171:628-41. e26.

[20] McGettrick A F, O'Neill L A. Localisation and trafficking of Toll-like receptors: an important mode of regulation. *Curr Opin Immunol*. 2010;22:20-27.

[21] Leifer C A, Medvedev A E. Molecular mechanisms of regulation of Toll-like receptor signaling. *J Leukoc Biol*. 2016;100:927-41.

[22] Xiao L, Li X-X, Chung H K, Kalakonda S, Cai J-Z, Cao S, et al. RNA-binding protein HuR regulates Paneth cell function by altering membrane localization of TLR2 via post-transcriptional control of CNPY3. *Gastroenterology*. 2019;157:731-43.

[23] Lee B L, Barton G M. Trafficking of endosomal Toll-like receptors. *Trends Cell Biol*. 2014;24:360-69.

[24] Chen X, Cubillos-Ruiz J R. Endoplasmic reticulum stress signals in the tumour and its microenvironment. *Nat Rev Cancer*. 2021;21:71-88.

[25] Bhattarai K R, Riaz T A, Kim H-R, Chae H-J. The aftermath of the interplay between the endoplasmic reticulum stress response and redox signaling. *Experimental & molecular medicine*. 2021;53:151-67.

[26] Volpi V G, Touvier T, D'Antonio M. Endoplasmic reticulum protein quality control failure in

myelin disorders. *Front Mol Neurosci.* 2017;9:162.

[27] Lemberg M K, Strisovsky K. Maintenance of organellar protein homeostasis by ER-associated degradation and related mechanisms. *Molecular Cell.* 2021;81:2507-19.

[28] Barker M, Rayens W. Partial least squares for discrimination. *J Chemom.* 2003;17:166-73.

[29] Su P, Wang Q, Bi E, Ma X, Liu L, Yang M, et al. Enhanced lipid accumulation and metabolism are required for the differentiation and activation of tumor-associated macrophages. *Cancer Res.* 2020;80:1438-50.

[30] Luo Q, Zheng N, Jiang L, Wang T, Zhang P, Liu Y, et al. Lipid accumulation in macrophages confers protumorigenic polarization and immunity in gastric cancer. *Cancer Sci.* 2020;111:4000-11.

[31] Feng M, Jiang W, Kim B Y, Zhang C C, Fu Y-X, Weissman I L. Phagocytosis checkpoints as new targets for cancer immunotherapy. *Nature Reviews Cancer.* 2019;19:568-86.

[32] Qi L, Tsai B, Arvan P. New insights into the physiological role of endoplasmic reticulum-associated degradation. *Trends Cell Biol.* 2017;27:430-40.

[33] Kwon D, Kim S-M, Correia M A. Cytochrome P450 endoplasmic reticulum-associated degradation (ERAD): therapeutic and pathophysiological implications. *Acta Pharm Sin B.* 2020;10:42-60.

[34] Zhang X, Goncalves R, Mosser D M. The isolation and characterization of murine macrophages. *Curr Protoc Immunol.* 2008;83:14.1. 1-14.1. 14.

704 **Acknowledgements**

705 The authors would like to thank Dr. Yong Jiang (Southern Medical University, Guangzhou, China) for
706 *Tlr2* KO C57BL/6J mice (Jackson Laboratory, #004650), Dr. Kui Cheng (Southern Medical University)
707 for providing SMU-Z1, Dr. Zhinan Yin (Jinan University, Guangzhou, China) for *Lyz2^{cre}* C57BL/6J
708 mice (Jackson Laboratory, #004781).

709 **Authors' contributions**

710 Rong-Rong He conceived and designed the experiments. Xiang Luo performed the experiments and
711 prepared the manuscript. Zi-Chun Li, Dong-Dong Li, Zi-Xuan Li, Chang-Yu Yan, Rui-Ting Huang Shu-
712 Rui Chen assisted the experiments and data analysis. Hai-Biao Gong, Rong Wang, Wan-Yang Sun
713 conducted and analyzed the LC–MS/MS-based experiments. Yue Feng and Mingxian Liu conducted the
714 synthesis of mPEG-PCL-SSZ micelles. Yun-Feng Cao supported the LC-MS platform and consulted
715 the data analysis. Lei Liang, Wen-Jun Duan, Feng Huang, Hiroshi Hurihara and Wen Jin advised the
716 project and revised the manuscript. Rong-Rong He, Yan-Ping Wu and Yi-Fang Li revised and approved
717 the manuscript. All authors read and approved the final manuscript.

718 **Funding**

719 This work was supported, in part, by Natural Science Foundation of China (82125038, T2341004,
720 82004231, 81903821, 81973718, 82274403, 82305063), Guangdong Basic and Applied Basic Research
721 Foundation (2021B1515120023, 2020A1515110388, 2021A1515011297, 2023B1515040016), the
722 Local Innovative and Research Teams Project of Guangdong Pearl River Talents Program
723 (2017BT01Y036) and GDUPS (2019), Innovation Team Project of Guangdong Provincial Department
724 of Education (2020KCXTD003), Medical Science and Technology Research Foundation of Guangdong
725 Province (A2023044), Fellowship of China Postdoctoral Science Foundation (2022TQ0122,
726 2023M731327), and Lift Project of Guangdong Second Provincial General Hospital (TJGC-2022002,
727 2022BSGZ007).

728 **Conflict of interest**

729 The authors declare no competing interests.

730 **Study approval**

731 All animal experiment protocols were undertaken in accordance with the National Institutes of Health's
732 Guide for the Care and Use of Laboratory Animals and were approved by the Laboratory Animal Ethic
733 Committee of Jinan University (approval number: IACUC-20220613-09).

734

735

736

737 Figure legends

738 **Fig. 1 Phospholipid peroxidation of macrophages provokes tumor resistance to ferroptosis**
 739 **therapy.** (a) Photographs of excised tumors (Scale = 1 cm), (b) tumor weight, and (c) tumor growth of
 740 C57BL/6J mice following intravenous administration of saline or mPEG-PCL-SSZ (equivalent to 40
 741 mg SSZ kg⁻¹) (*n* = 6). The phospholipids in TME macrophages were isolated and detected by LC-
 742 MS/MS (*n* = 3). Data of phospholipids were extracted and displayed as (d) Orthogonal partial least
 743 squares discriminant analysis (OPLS-DA), (e) heatmap and (f-g) volcano plots showing the fold
 744 changes (X-axis) versus significance (Y-axis). (i) Tumor weight, (j) photographs of excised tumors
 745 (Scale = 1 cm), (k) tumor growth and (l) relative tumor weight reduction of *Gpx4*^{CKO} C57BL/6J mice
 746 following intravenous administration of saline or mPEG-PCL-SSZ (equivalent to 40 mg SSZ kg⁻¹) (*n*
 747 = 6). (m) Photographs of excised tumors (Scale = 1 cm). (n) tumor growth, (o) tumor weight and (p)
 748 relative tumor weight reduction of WT or *Gpx4*^{CKO} C57BL/6J mice with RSL3 (100 mg/kg)
 749 intratumorally administration (*n* = 6). (q) 4-HNE protein expression in macrophages was detected by
 750 F4/80 and 4-HNE double immunostaining in tumor tissues. Scale = 50 μm. The values are represented
 751 as mean ± SD. The *p*-values were determined by two-way repeated measures ANOVA [(d), (k), (n)],
 752 one-way ANOVA with LSD post hoc test (o), or independent samples *t*-test [(a), (b), (g-i), (l), (p)]. **P*
 753 < 0.05, ***P* < 0.01, ****P* < 0.001.

754
 755 **Fig. 2 Phospholipid peroxidation of macrophages impairs phagocytic clearance of ferroptotic**
 756 **tumor cells.** (a) and (b) IHC analysis of tumor tissue section stained with F4/80 and hematoxylin from
 757 WT and *Gpx4*^{CKO} C57BL/6J mice. The phagocytosis of tumor cells by macrophages in tumor tissues
 758 was observed and indicated by red arrow. Scale = 50 μm (top panels) and 10 μm (bottom panels). (c)
 759 Schematic representation of phospholipid peroxidation metabolic pathways and inducers. (d) THP1
 760 macrophages were treated with different concentrations of RSL3 (0, 0.125, 0.25 and 0.5 μM) for 6 h
 761 and cocultured with ferroptotic HL60 cells (pretreated with RSL3 (1 μM, 6 h)) for 2 h. (e) THP1
 762 macrophages were treated with lipid peroxidation inhibitors (ferrostatin-1 (Fer1), 2 μM, 2 h;
 763 deferoxamine (DFO), 100 μM, 2 h; N-Acetyl Cysteine (NAC), 5 mM, 2 h;) and RSL3 (0.5 μM) for 6 h
 764 before incubation with ferroptotic HL60 cells. (f-g) BMDMs were treated with Fer-1 (2 μM, 2 h) and
 765 RSL3 (0.5 μM) for 6 h before incubation with ferroptotic L1210 cells cells (pretreated with RSL3 (2.5

766 μM , 6 h)). Scale = 50 μm (top panels) and 10 μm (bottom panels). (h) GPX4 expression in siGPX4s
767 treated THP1 macrophages were confirmed by western blotting analysis. (i) Phagocytosis of siGPX4s-
768 treated THP1 macrophages to ferroptotic HL60 cells. (j) Phagocytosis of ferroptotic L1210 cells by
769 BMDMs from WT and *Gpx4*^{CKO} C57BL/6J mice. (k) Representative phagocytosis of ferroptotic L1210
770 cells by BMDMs from WT and *Gpx4*^{CKO} C57BL/6J mice. Scale = 50 μm (top panels) and 10 μm (bottom
771 panels). (l) THP1 macrophages treated with supplementary LA (20 μM , 16 h) and RSL3 (0.5 μM , 6 h).
772 (m) THP1 macrophages were treated with dose-dependent of Erastin (0, 0.25, 0.5 and 1 μM) for 12 h
773 and cocultured with ferroptotic HL60 cells for 2 h. The phagocytosis was measured by flow cytometry
774 and confocal microscopy. The values are represented as mean \pm SD ($n = 5$). The p -values were
775 determined by one-way ANOVA with LSD post hoc test [(d-f), (h-i), (m)], or independent samples t -
776 test [(j), (l)]. ** $P < 0.01$, *** $P < 0.001$, # $P < 0.05$, ## $P < 0.01$, ### $P < 0.001$.

777

778 **Fig. 3 TLR2 plays an indispensable role in phospholipid peroxidation-provoked impairment of**
779 **ferroptotic cell clearance and tumor resistance to ferroptosis therapy.** (a) Schematic protocol for
780 WT and *Tlr2* KO C57BL/6J mice bearing E0771 tumor. (b) Tumor growth, (c) tumor weight and (d)
781 relative tumors weight reduction of WT and *Tlr2* KO C57BL/6J mice after RSL3 (100 mg/kg)
782 intratumorally administrated twice each week for two consecutive weeks ($n = 6$). (e) Photographs of
783 excised E0771 solid tumors on 16th day. Scale = 1 cm. (f) M1-like macrophages were monitored by
784 F4/80 and iNOS double immunostaining in tumor tissues. The phagocytosis of tumor cells by
785 macrophages in tumor tissues was observed and indicated by white arrow. Scale = 50 μm (left panels)
786 and 10 μm (right panels). (g) IHC analysis of tumor tissue section stained with F4/80 and hematoxylin
787 from WT and *Tlr2* KO C57BL/6J mice. The phagocytosis of tumor cells by macrophages in tumor
788 tissues was observed and indicated by red arrow. Scale = 50 μm (top panels) and 10 μm (bottom panels).
789 (h) TLR2 expression in BMDMs from WT and *Tlr2* KO C57BL/6J mice was detected by western
790 blotting analysis. (i) Phagocytosis of BMDMs from WT and *Tlr2* KO C57BL/6J mice treated with dose-
791 dependent RSL3 (0, 0.125, 0.25 and 0.5 μM) for 6 h ($n = 5$). (j) Phagocytosis of ferroptotic L1210 cells
792 by BMDMs from WT and *Tlr2* KO C57BL/6J mice was assessed by confocal microscopy. Scale = 50
793 μm (top panels) and 10 μm (bottom panels). The values are represented as mean \pm SD. The p -values
794 were determined by two-way repeated measures ANOVA (b), one-way ANOVA with LSD post hoc test

[(c), (i)], or independent samples *t*-test (d). **P* < 0.05, ***P* < 0.01, ****P* < 0.001, #*P* < 0.05.

Fig. 4 Oxygenated PE disrupts the translocation of TLR2 from ER to PM by inhibiting the interaction between TLR2 and CNPY3. (a) THP1 macrophages were treated with Fer-1 (2 μM, 2 h) and RSL3 (0.5 μM) for 6 h. The gene expressions of *TLR2* were determined by qPCR assay (*n* = 5). (b) The protein expression of TLR2 in THP1 macrophages were detected by western blotting analysis (*n* = 3). (c) TLR2 distribution in PM and cytoplasm (including cytosol fraction and organelles) fractions of RSL3 treated THP1 macrophages were detected by western blotting analysis (*n* = 3). (d) The ER of THP1 macrophages was isolated and identified with multiple biofilm markers. (e) TLR2 distribution in ER fractions of RSL3 (0.5 μM, 6h) treated THP1 macrophages were detected by western blotting analysis (extracted fractions were immunoblotted along with total proteins of whole cell) (*n* = 3). (f) TLR2 and E-cadherin colocalization analysis in RSL3 (0.5 μM, 6h) treated THP1 macrophages were assessed by confocal microscopy. Scale = 5 μm. (g) TLR2 and Calnexin colocalization analysis in RSL3 (0.5 μM, 6 h) treated THP1 macrophages were assessed by confocal microscopy. Scale = 5 μm. (h) Experimental schema for establishing ER-specific oxPEs accumulation by transfection of ER-targeted ALOX15/PEBP1. (i) TLR2 distribution in PM, Cyt and (j) ER fractions in HEK293 cells transfected with ER-targeted pcDNA3.1-PEBP1-HA and pcDNA3.1-ALOX15-Flag for 24 h were detected by western blotting analysis (*n* = 3). (k) Co-immunoprecipitation assays of TLR2 and CNPY3 in RSL3 (0.5 μM, 6h) and Fer-1 (2 μM, 2 h) treated THP1 macrophages. Whole lysates were subjected to immunoprecipitation with TLR2 or CNPY3 antibody attached to sepharose. Immunoprecipitates and Whole-cell lysates were analyzed by immunoblotting with an TLR2 or CNPY3 antibody (*n* = 3). (l) Schematic representation of oxygenated PE disrupted PM trafficking of TLR2 by attenuating the interaction between TLR2 and CNPY3. The values are represented as mean ± SD. The *p*-values were determined by one-way ANOVA with LSD post hoc test [(a-b), (k)], or independent samples *t*-test [(e), (i-j)]. **P* < 0.05, ***P* < 0.01, ###*P* < 0.01.

Fig. 5 OxPEs in ER mediates proteasome-dependent degradation of TLR2. THP1 macrophages were treated with RSL3 (0.5 μM) for different time periods (0, 6, 12, 24 and 48 h). (a) The gene expressions of *TLR2* were determined by qPCR assay (*n* = 5). (b) The protein expression of TLR2 in

THP1 macrophages were detected by western blotting analysis ($n = 3$). (c) The protein expressions of TLR2 in WT and *Gpx4*^{CKO} BMDMs were detected by western blotting analysis ($n = 3$). (d) THP1 macrophages were treated with or without RSL3 (0.5 μ M) for 24 h in the presence of CHX (25 μ M), and the protein expression of TLR2 was detected by western blotting analysis ($n = 3$). (e) THP1 macrophages were treated with or RSL3 (0.5 μ M) for 48 h, and then treated with MG132 (10 μ M) or 3-MA (10 μ M) for 12 h. TLR2 protein expression were determined by western blotting analysis ($n = 3$). (f) THP1 macrophages were treated with Fer-1 (2 μ M) and RSL3 (0.5 μ M) for 48 h, and then the levels of TLR2 ubiquitination were analyzed by western blotting ($n = 3$). THP1 macrophages transfected with ER-targeted pcDNA3.1-PEBP1-HA and pcDNA3.1-ALOX15-Flag for 48 h. (g) The protein expression of TLR2 and (h) the levels of TLR2 ubiquitination were detected by western blotting analysis ($n = 3$). (i) The phagocytosis was measured by flow cytometry ($n = 5$). The values are represented as mean \pm SD. The p -values were determined by two-way repeated measures ANOVA (d), one-way ANOVA with LSD post hoc test [(a-b), (e-f)], or independent samples t -test [(c), (g-i)]. * $P < 0.05$, ** $P < 0.01$, *** $P < 0.001$, # $P < 0.05$, ## $P < 0.01$.

Fig. 6 Identification of MARCH6 as a key E3 ligase in oxPEs-induced ubiquitin-dependent degradation of TLR2. (a-e) HEK293 cells transfected with ER-targeted pcDNA3.1-PEBP1-HA, ER-targeted pcDNA3.1-ALOX15-Flag and pcDNA3.1-TLR2-Myc for 48 h. (a) Co-immunoprecipitation assays of TLR2 and MARCH6 ($n = 3$). Whole lysates were subjected to immunoprecipitation with Myc or His antibody attached to sepharose. Immunoprecipitates and whole-cell lysates were analyzed by immunoblotting with an Myc or His antibody. (b) MARCH6 expression in siMARCH6s treated HEK293 cells were confirmed by western blotting analysis. (c) TLR2 protein level and (d) its ubiquitination level were measured after siRNA-mediated knockdown of MARCH6 in HEK293 cells ($n = 3$). (e) TLR2 protein level and (f) its ubiquitination level were evaluated in MARCH6 overexpressed HEK293 cells ($n = 3$). The values are represented as mean \pm SD. The p -values were determined independent samples t -test (A), the p -values were determined by one-way ANOVA with LSD post hoc test (b-e). * $P < 0.05$, ** $P < 0.01$, *** $P < 0.001$, # $P < 0.05$, ## $P < 0.01$.

Fig. 7 SAPE-OOH serves as a crucial oxidized phospholipid for TLR2 ubiquitination. HEK293

cells transfected with ER-targeted ALOX15 and PEBP1 plasmid for 48 h, and then ER fractions were isolated and measured by LC/MS/MS-based phospholipidomics. (a) Assessment of oxygenated phospholipids by LC/MS/MS and visualized by heatmap ($n = 5$). Multivariate statistical analysis of (b) oxPLs and (c) oxPEs using OPLS-DA analysis between transfection of vector and ER-targeted ALOX15/PEBP1 plasmids in HEK293 cells. Each point represents a sample ($n = 5$). (d) Dot plots demonstrating variable importance for prediction scores of various oxPLs species in distinguishing between vector and ER-targeted ALOX15/PEBP1-transfected HEK293 cells ($n = 5$). Obtained data were visualized as volcano plots and displayed the changes in the levels of oxygenated phospholipids (\log_2 (ALOX15/PEBP1)/Vector), X-axis) vs significance ($-\log_{10}$ (P -value), Y-axis). (e) Each dot represents a class of oxPLs. (f) 1O, 2O and 3O, indicate singly, doubly, and triply oxPLs, respectively. (g) THP1 macrophages treated with SAPE (4 μ M) or SAPE-OOH (4 μ M) for 24 h and the levels of TLR2 ubiquitination measured by western blotting analysis ($n = 3$). (h) THP1 macrophages treated with dose-dependent enrichment of SAPE or SAPE-OOH for 24 h and phagocytosis was measured by flow cytometry ($n = 5$). The values are represented as mean \pm SD. The p -values were determined independent samples t -test [(e-g), (h)], one-way ANOVA with LSD post hoc test (i). ** $P < 0.01$, *** $P < 0.001$.

Fig. 8 TLR2 agonist enhances the antitumor efficacy of ferroptosis inducer. (a) Schematic protocol for C57BL/6J mice bearing E0771 tumor. E0771 cells were mixed with or without SMU-Z1-pretreated *Gpx4*^{CKO} BMDM macrophages at a ratio of 5:1 and then injected subcutaneously into C57BL/6J mice, and then RSL3 (50 mg/kg) intratumorally administrated twice each week for two consecutive weeks. (b) Photographs of excised E0771 solid tumors (Scale = 1 cm). (c) Tumor weight, (d) relative reduction of tumor weight and (e) tumor growth of E0771 bearing mice ($n = 6$). (f) TLR2 protein expression in tumor tissues were detected by western blotting analysis ($n = 3$). (g) Immunofluorescence analysis of M1-like macrophages were monitored by F4/80 and iNOS double immunostaining in tumor tissues. The phagocytosis of tumor cells by macrophages in tumor tissues was observed and indicated by white arrow. Scale = 50 μ m (left panels) and 10 μ m (right panels). (h) THP1 macrophages were treated with SMU-Z1 (1 μ M, 24 h) and RSL3 (0.5 μ M, 6 h), and then phagocytosis was measured by flow cytometry ($n = 5$). The values are represented as mean \pm SD. The p -values were determined by one-way ANOVA with LSD post hoc test (c), two-way repeated measures ANOVA (e), or independent samples t -test [(d), (f),

882 (h)]. $*P < 0.05$, $**P < 0.01$, $***P < 0.001$, $##P < 0.01$, $###P < 0.001$, $@@@P < 0.001$.

883

Figures

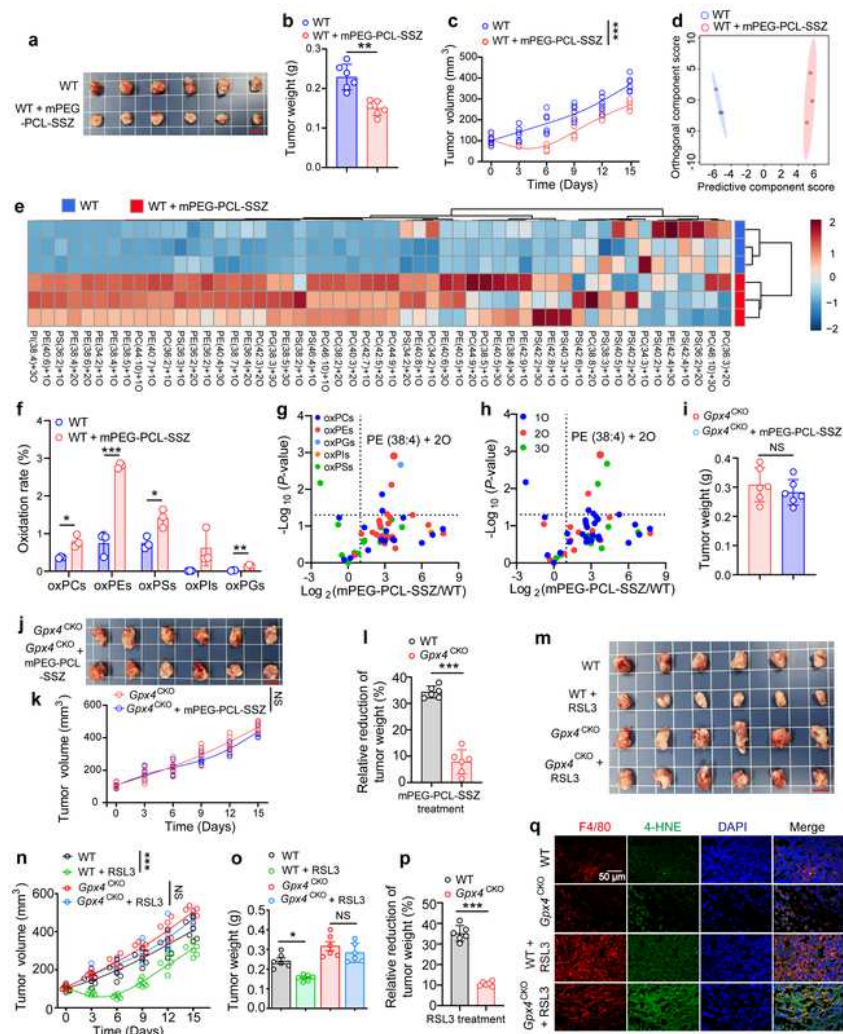


Fig. 1 Phospholipid peroxidation of macrophages provokes tumor resistance to ferroptosis therapy. (a) Photographs of excised tumors (Scale = 1 cm), (b) tumor weight, and (c) tumor growth of C57BL/6J mice following intravenous administration of saline or mPEG-PCL-SSZ (equivalent to 40 mg SSZ kg⁻¹) (*n* = 6). The phospholipids in TME macrophages were isolated and detected by LC-MS/MS (*n* = 3). Data of phospholipids were extracted and displayed as (d) Orthogonal partial least squares discriminant analysis (OPLS-DA), (e) heatmap and (f-g) volcano plots showing the fold changes (X-axis) versus significance (Y-axis). (i) Tumor weight, (j) photographs of excised tumors (Scale = 1 cm), (k) tumor growth and (l) relative tumor weight reduction of *Gpx4*^{CKO} C57BL/6J mice following intravenous administration of saline or mPEG-PCL-SSZ (equivalent to 40 mg SSZ kg⁻¹) (*n* = 6). (m) Photographs of excised tumors (Scale = 1 cm), (n) tumor growth, (o) tumor weight and (p) relative tumor weight reduction of WT or *Gpx4*^{CKO} C57BL/6J mice with RSL3 (100 mg/kg) intratumorally administration (*n* = 6). (q) 4-HNE protein expression in macrophages was detected by F4/80 and 4-HNE double immunostaining in tumor tissues. Scale = 50 μm. The values are represented as mean ± SD. The *p*-values were determined by two-way repeated measures ANOVA [(d), (k), (n)], one-way ANOVA with LSD post hoc test (o), or independent samples *t*-test [(a), (b), (g-i), (l), (p)]. **P* < 0.05, ***P* < 0.01, ****P* < 0.001.

Figure 1

See image above for figure legend.

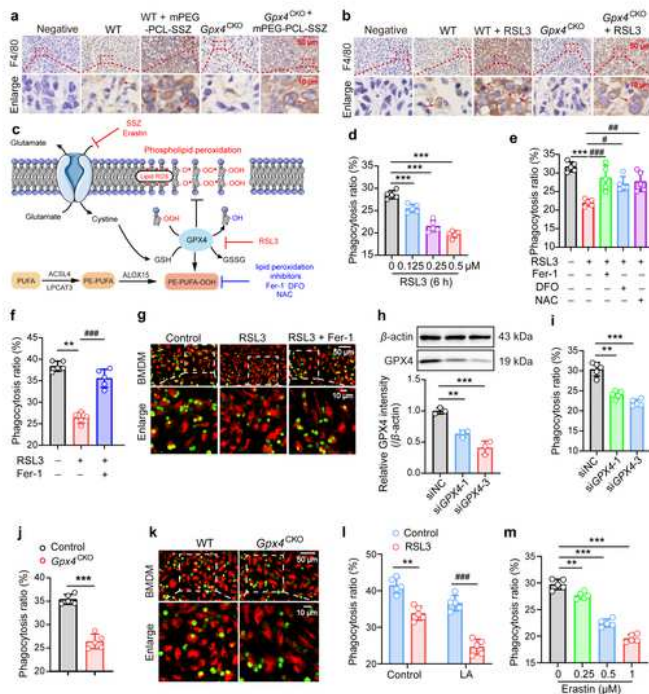


Fig. 2 Phospholipid peroxidation of macrophages impairs phagocytic clearance of ferroptotic tumor cells. (a) and (b) IHC analysis of tumor tissue section stained with F4/80 and hematoxylin from WT and *Gpx4*^{KO} C57BL/6J mice. The phagocytosis of tumor cells by macrophages in tumor tissues was observed and indicated by red arrow. Scale = 50 μ m (top panels) and 10 μ m (bottom panels). (c) Schematic representation of phospholipid peroxidation metabolic pathways and inducers. (d) THP1 macrophages were treated with different concentrations of RSL3 (0, 0.125, 0.25 and 0.5 μ M) for 6 h and cocultured with ferroptotic HL60 cells (pretreated with RSL3 (1 μ M, 6 h)) for 2 h. (e) THP1 macrophages were treated with lipid peroxidation inhibitors (ferrostatin-1 (Fer1), 2 μ M, 2 h; deferoxamine (DFO), 100 μ M, 2 h; N-Acetyl Cysteine (NAC), 5 mM, 2 h;) and RSL3 (0.5 μ M) for 6 h before incubation with ferroptotic HL60 cells. (f-g) BMDMs were treated with Fer-1 (2 μ M, 2 h) and RSL3 (0.5 μ M) for 6 h before incubation with ferroptotic L1210 cells (pretreated with RSL3 (2.5

μ M, 6 h)). Scale = 50 μ m (top panels) and 10 μ m (bottom panels). (h) GPX4 expression in siGPX4s treated THP1 macrophages were confirmed by western blotting analysis. (i) Phagocytosis of siGPX4s-treated THP1 macrophages to ferroptotic HL60 cells. (j) Phagocytosis of ferroptotic L1210 cells by BMDMs from WT and *Gpx4*^{KO} C57BL/6J mice. (k) Representative phagocytosis of ferroptotic L1210 cells by BMDMs from WT and *Gpx4*^{KO} C57BL/6J mice. Scale = 50 μ m (top panels) and 10 μ m (bottom panels). (l) THP1 macrophages treated with supplementary LA (20 μ M, 16 h) and RSL3 (0.5 μ M, 6 h). (m) THP1 macrophages were treated with dose-dependent of Erastin (0, 0.25, 0.5 and 1 μ M) for 12 h and cocultured with ferroptotic HL60 cells for 2 h. The phagocytosis was measured by flow cytometry and confocal microscopy. The values are represented as mean \pm SD ($n = 5$). The p -values were determined by one-way ANOVA with LSD post hoc test [(d-f), (h-i), (m)], or independent samples t -test [(j), (l)]. ** $P < 0.01$, *** $P < 0.001$, [#] $P < 0.05$, ^{##} $P < 0.01$, ^{###} $P < 0.001$.

Figure 2

See image above for figure legend.

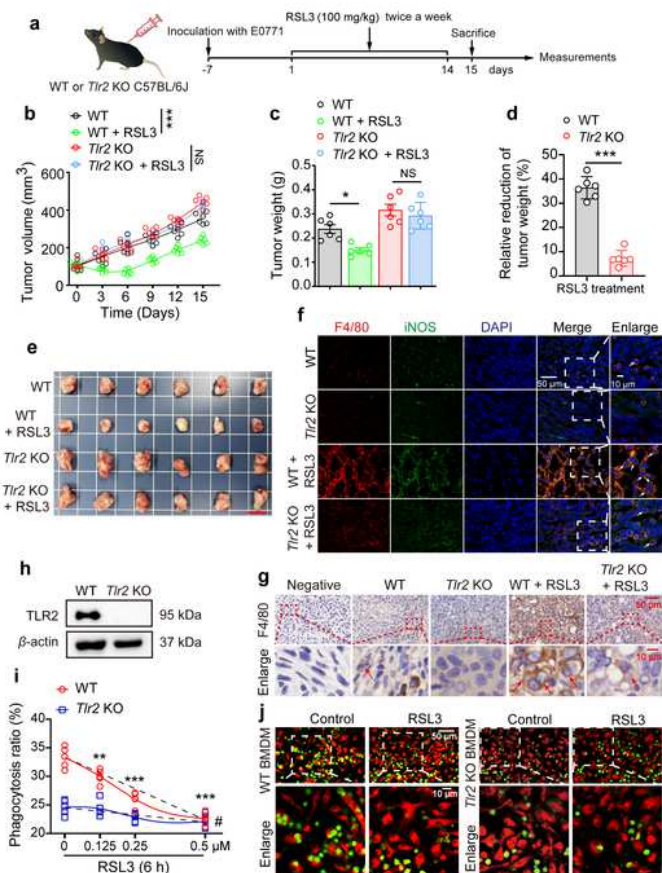


Fig. 3 TLR2 plays an indispensable role in phospholipid peroxidation-provoked impairment of ferroptotic cell clearance and tumor resistance to ferroptosis therapy. (a) Schematic protocol for WT and *Tlr2* KO C57BL/6J mice bearing E0771 tumor. (b) Tumor growth, (c) tumor weight and (d) relative tumors weight reduction of WT and *Tlr2* KO C57BL/6J mice after RSL3 (100 mg/kg) intratumorally administrated twice each week for two consecutive weeks ($n = 6$). (e) Photographs of excised E0771 solid tumors on 16th day. Scale = 1 cm. (f) M1-like macrophages were monitored by F4/80 and iNOS double immunostaining in tumor tissues. The phagocytosis of tumor cells by macrophages in tumor tissues was observed and indicated by white arrow. Scale = 50 μm (left panels) and 10 μm (right panels). (g) IHC analysis of tumor tissue section stained with F4/80 and hematoxylin from WT and *Tlr2* KO C57BL/6J mice. The phagocytosis of tumor cells by macrophages in tumor tissues was observed and indicated by red arrow. Scale = 50 μm (top panels) and 10 μm (bottom panels). (h) TLR2 expression in BMDMs from WT and *Tlr2* KO C57BL/6J mice was detected by western blotting analysis. (i) Phagocytosis of BMDMs from WT and *Tlr2* KO C57BL/6J mice treated with dose-dependent RSL3 (0, 0.125, 0.25 and 0.5 μM) for 6 h ($n = 5$). (j) Phagocytosis of ferroptotic L1210 cells by BMDMs from WT and *Tlr2* KO C57BL/6J mice was assessed by confocal microscopy. Scale = 50 μm (top panels) and 10 μm (bottom panels). The values are represented as mean \pm SD. The p -values were determined by two-way repeated measures ANOVA (b), one-way ANOVA with LSD post hoc test [(c), (f)], or independent samples t -test [(d), (g), (i), (j)]. * $P < 0.05$, ** $P < 0.01$, *** $P < 0.001$, # $P < 0.05$.

Figure 3

See image above for figure legend.

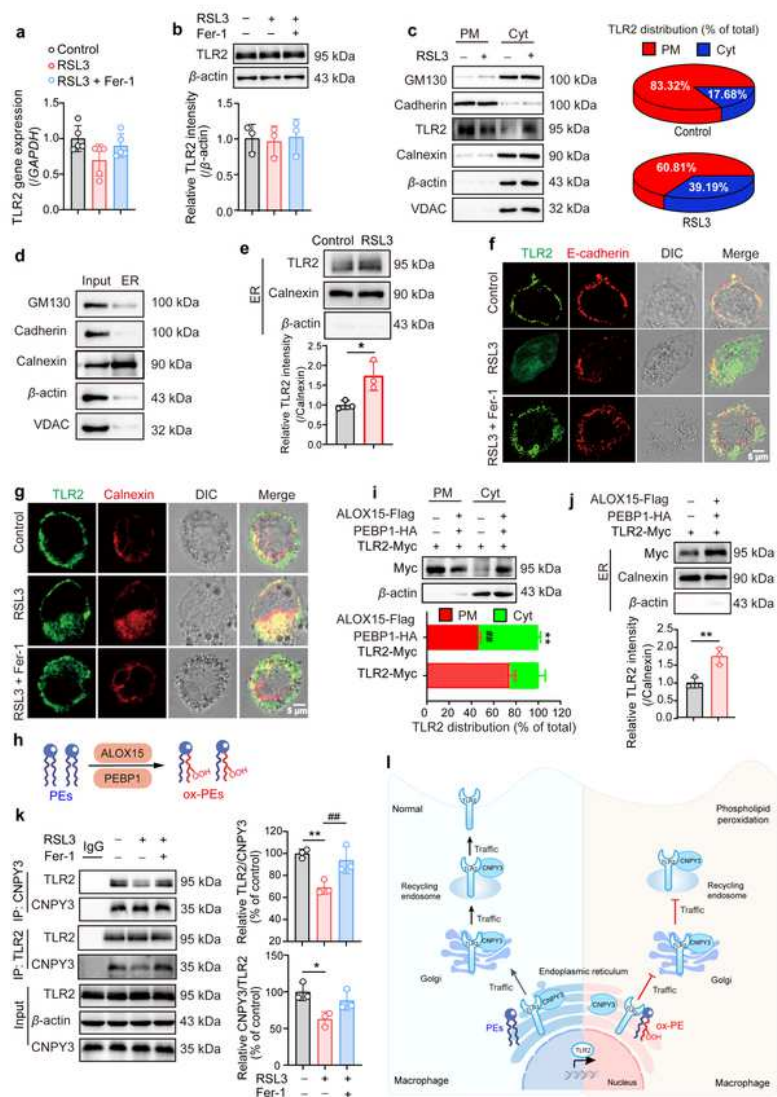


Fig. 4 Oxygenated PE disrupts the translocation of TLR2 from ER to PM by inhibiting the interaction between TLR2 and CNPY3. (a) THP1 macrophages were treated with Fer-1 (2 μ M, 2 h) and RSL3 (0.5 μ M) for 6 h. The gene expressions of *TLR2* were determined by qPCR assay ($n = 5$). (b) The protein expression of TLR2 in THP1 macrophages were detected by western blotting analysis ($n = 3$). (c) TLR2 distribution in PM and cytoplasm (including cytosol fraction and organelles) fractions of RSL3 treated THP1 macrophages were detected by western blotting analysis ($n = 3$). (d) The ER of THP1 macrophages was isolated and identified with multiple biofilin markers. (e) TLR2 distribution in ER fractions of RSL3 (0.5 μ M, 6 h) treated THP1 macrophages were detected by western blotting analysis (extracted fractions were immunoblotted along with total proteins of whole cell) ($n = 3$). (f) TLR2 and E-cadherin colocalization analysis in RSL3 (0.5 μ M, 6 h) treated THP1 macrophages were assessed by confocal microscopy. Scale = 5 μ m. (g) TLR2 and Calnexin colocalization analysis in RSL3 (0.5 μ M, 6 h) treated THP1 macrophages were assessed by confocal microscopy. Scale = 5 μ m. (h) Experimental schema for establishing ER-specific oxPEs accumulation by transfection of ER-targeted ALOX15/PEBP1. (i) TLR2 distribution in PM, Cyt and (j) ER fractions in HEK293 cells transfected with ER-targeted pcDNA3.1-PEBP1-HA and pcDNA3.1-ALOX15-Flag for 24 h were detected by western blotting analysis ($n = 3$). (k) Co-immunoprecipitation assays of TLR2 and CNPY3 in RSL3 (0.5 μ M, 6 h) and Fer-1 (2 μ M, 2 h) treated THP1 macrophages. Whole lysates were subjected to immunoprecipitation with TLR2 or CNPY3 antibody attached to sepharose. Immunoprecipitates and Whole-cell lysates were analyzed by immunoblotting with an TLR2 or CNPY3 antibody ($n = 3$). (l) Schematic representation of oxygenated PE disrupting PM trafficking of TLR2 by attenuating the interaction between TLR2 and CNPY3. The values are represented as mean \pm SD. The p -values were determined by one-way ANOVA with LSD post hoc test [(a-b), (d-k)], or independent samples *t*-test [(e), (i-j)]. * $P < 0.05$, ** $P < 0.01$, *** $P < 0.001$.

Figure 4

See image above for figure legend.

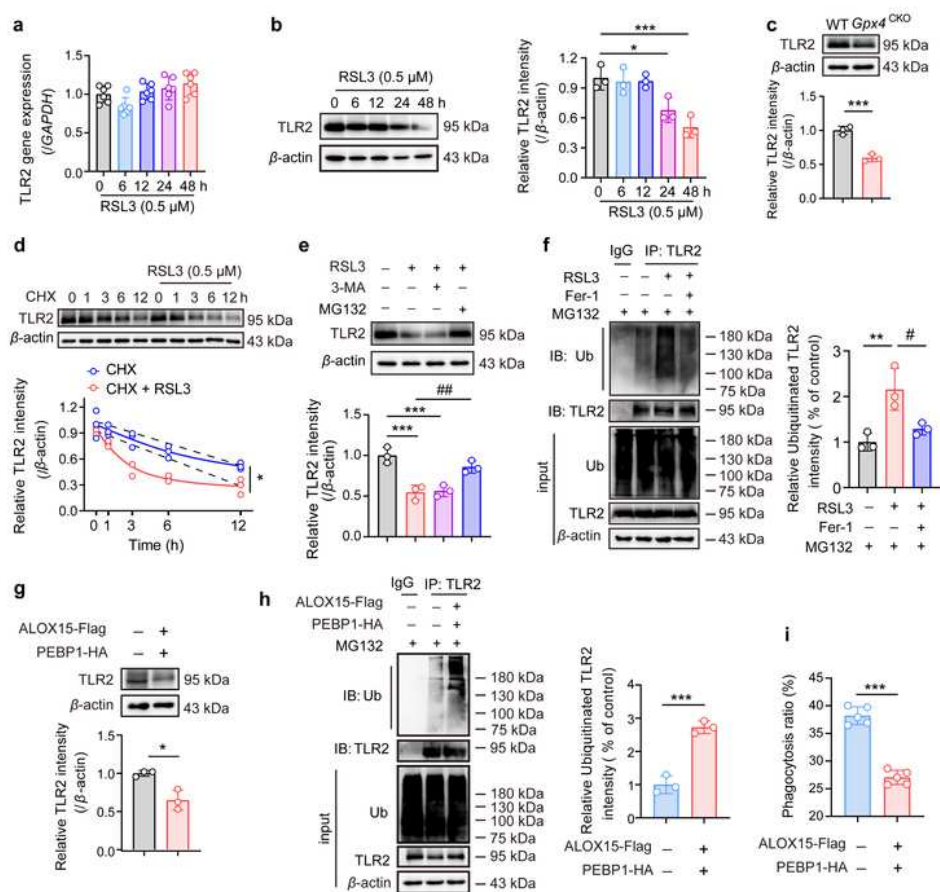


Fig. 5 OxPEs in ER mediates proteasome-dependent degradation of TLR2. THP1 macrophages were treated with RSL3 (0.5 μ M) for different time periods (0, 6, 12, 24 and 48 h). (a) The gene expressions of *TLR2* were determined by qPCR assay ($n = 5$). (b) The protein expression of TLR2 in

THP1 macrophages were detected by western blotting analysis ($n = 3$). (c) The protein expressions of TLR2 in WT and *Gpx4*^{CKO} BMDMs were detected by western blotting analysis ($n = 3$). (d) THP1 macrophages were treated with or without RSL3 (0.5 μ M) for 24 h in the presence of CHX (25 μ M), and the protein expression of TLR2 was detected by western blotting analysis ($n = 3$). (e) THP1 macrophages were treated with or without RSL3 (0.5 μ M) for 48 h, and then treated with MG132 (10 μ M) or 3-MA (10 μ M) for 12 h. TLR2 protein expression were determined by western blotting analysis ($n = 3$). (f) THP1 macrophages were treated with Fer-1 (2 μ M) and RSL3 (0.5 μ M) for 48 h, and then the levels of TLR2 ubiquitination were analyzed by western blotting ($n = 3$). THP1 macrophages transfected with ER-targeted pcDNA3.1-PEBP1-HA and pcDNA3.1-ALOX15-Flag for 48 h. (g) The protein expression of TLR2 and (h) the levels of TLR2 ubiquitination were detected by western blotting analysis ($n = 3$). (i) The phagocytosis was measured by flow cytometry ($n = 5$). The values are represented as mean \pm SD. The p -values were determined by two-way repeated measures ANOVA (d), one-way ANOVA with LSD post hoc test [(a-b), (e-f)], or independent samples t -test [(c), (g-i)]. * $P < 0.05$, ** $P < 0.01$, *** $P < 0.001$, **** $P < 0.0001$.

Figure 5

See image above for figure legend.

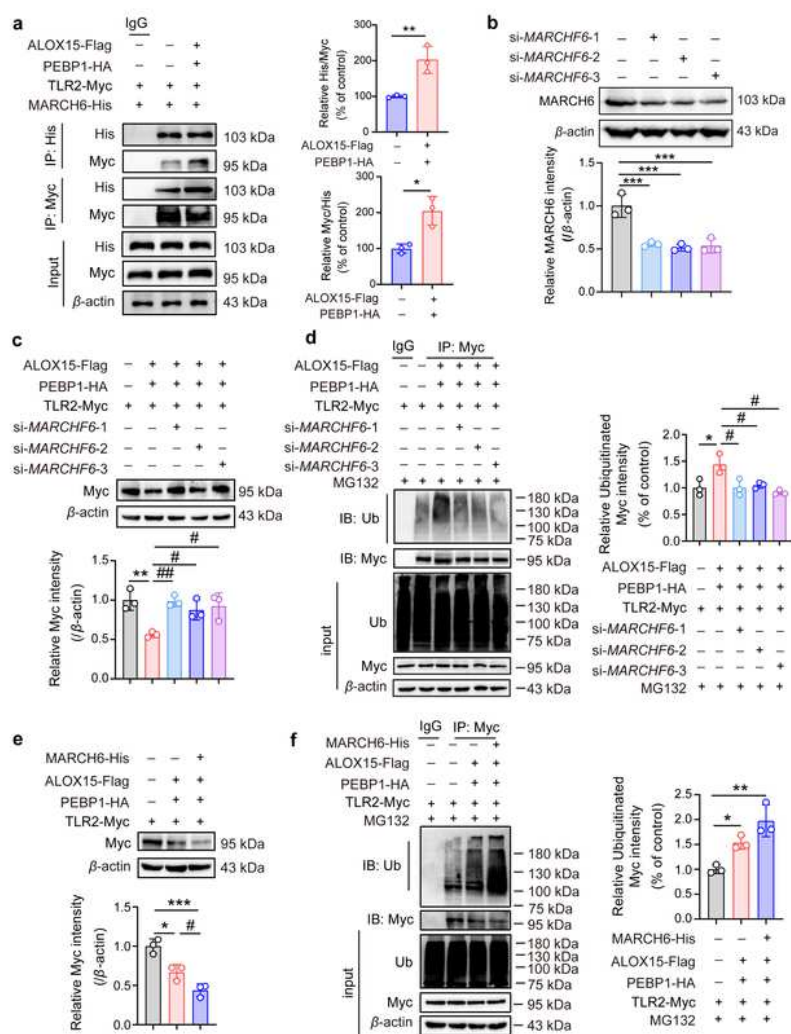


Fig. 6 Identification of MARCH6 as a key E3 ligase in oxPEs-induced ubiquitin-dependent degradation of TLR2. (a-e) HEK293 cells transfected with ER-targeted pcDNA3.1-PEBP1-HA, ER-targeted pcDNA3.1-ALOX15-Flag and pcDNA3.1-TLR2-Myc for 48 h. (a) Co-immunoprecipitation assays of TLR2 and MARCHF6 ($n = 3$). Whole lysates were subjected to immunoprecipitation with Myc or His antibody attached to sepharose. Immunoprecipitates and whole-cell lysates were analyzed by immunoblotting with an Myc or His antibody. (b) MARCH6 expression in siMARCHF6s treated HEK293 cells were confirmed by western blotting analysis. (c) TLR2 protein level and (d) its ubiquitination level were measured after siRNA-mediated knockdown of MARCHF6 in HEK293 cells ($n = 3$). (e) TLR2 protein level and (f) its ubiquitination level were evaluated in MARCHF6 overexpressed HEK293 cells ($n = 3$). The values are represented as mean \pm SD. The p -values were determined independent samples t -test (A), the p -values were determined by one-way ANOVA with LSD post hoc test (b-e). * $P < 0.05$, ** $P < 0.01$, *** $P < 0.001$, * $P < 0.05$, ** $P < 0.01$.

Figure 6

See image above for figure legend.

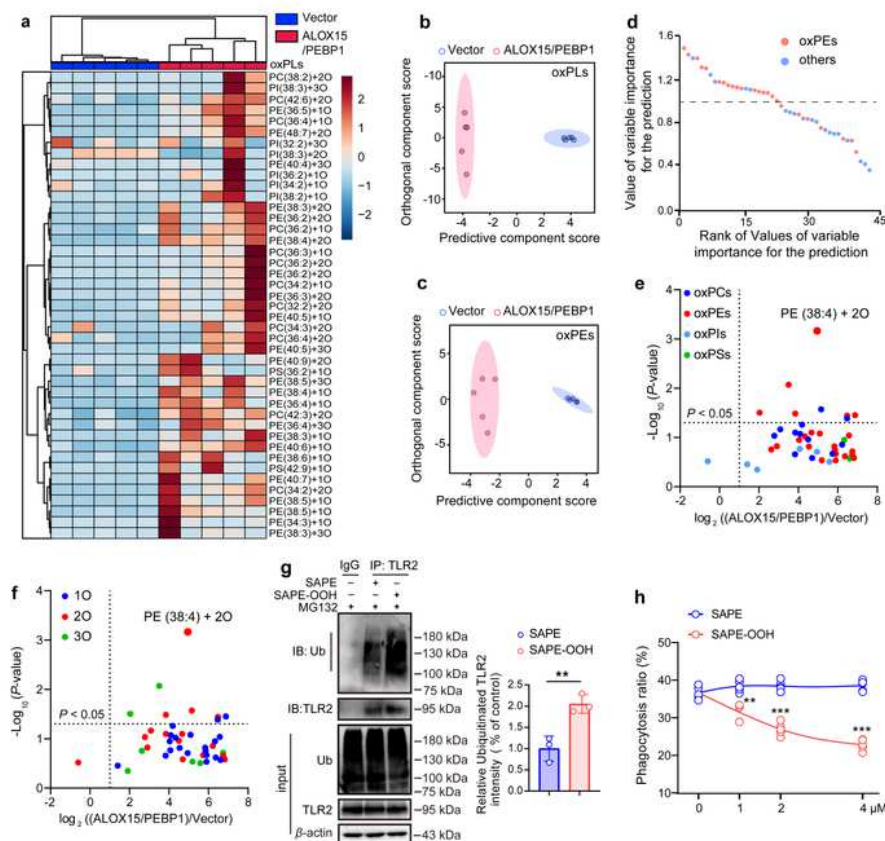


Fig. 7 SAPE-OOH serves as a crucial oxidized phospholipid for TLR2 ubiquitination. HEK293

cells transfected with ER-targeted ALOX15 and PEBP1 plasmid for 48 h, and then ER fractions were isolated and measured by LC/MS/MS-based phospholipidomics. (a) Assessment of oxygenated phospholipids by LC/MS/MS and visualized by heatmap ($n = 5$). Multivariate statistical analysis of (b) oxPLs and (c) oxPEs using OPLS-DA analysis between transfection of vector and ER-targeted ALOX15/PEBP1 plasmids in HEK293 cells. Each point represents a sample ($n = 5$). (d) Dot plots demonstrating variable importance for prediction scores of various oxPLs species in distinguishing between vector and ER-targeted ALOX15/PEBP1-transfected HEK293 cells ($n = 5$). Obtained data were visualized as volcano plots and displayed the changes in the levels of oxygenated phospholipids (\log_2 (ALOX15/PEBP1)/Vector, X-axis) vs significance ($-\log_{10}$ (P-value), Y-axis). (e) Each dot represents a class of oxPLs. (f) 1O, 2O and 3O, indicate singly, doubly, and triply oxPLs, respectively. (g) THP1 macrophages treated with SAPE (4 μ M) or SAPE-OOH (4 μ M) for 24 h and the levels of TLR2 ubiquitination measured by western blotting analysis ($n = 3$). (h) THP1 macrophages treated with dose-dependent enrichment of SAPE or SAPE-OOH for 24 h and phagocytosis was measured by flow cytometry ($n = 5$). The values are represented as mean \pm SD. The P -values were determined independent samples t -test [(e-g), (h)], one-way ANOVA with LSD post hoc test (i). ** $P < 0.01$, *** $P < 0.001$.

Figure 7

See image above for figure legend.

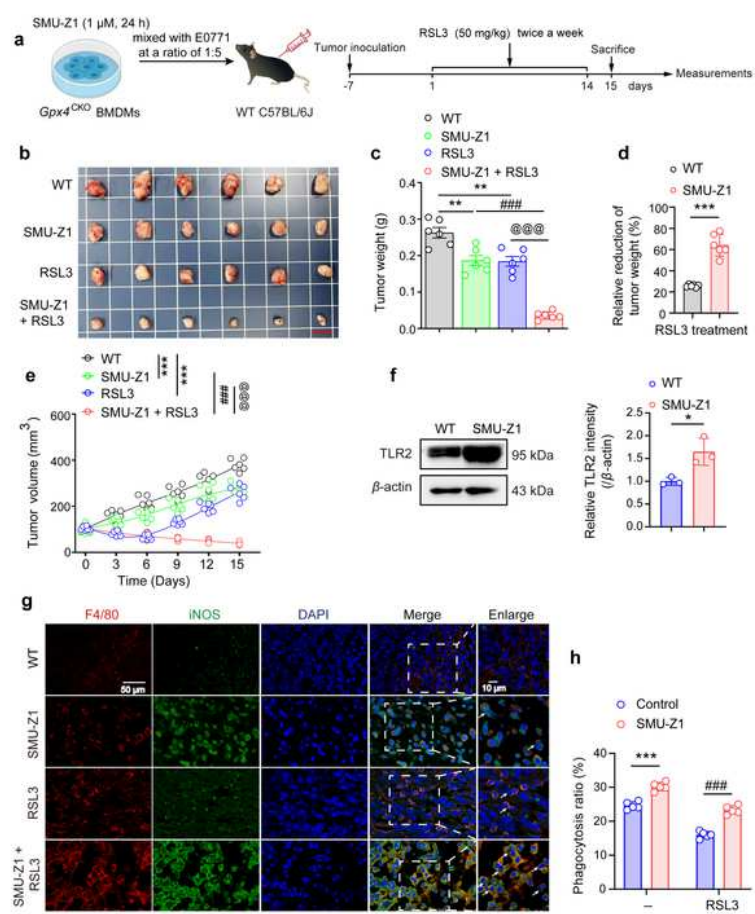


Fig. 8 TLR2 agonist enhances the antitumor efficacy of ferroptosis inducer. (a) Schematic protocol for C57BL/6J mice bearing E0771 tumor. E0771 cells were mixed with or without SMU-Z1-pretreated *Gpx4*^{CKO} BMDM macrophages at a ratio of 5:1 and then injected subcutaneously into C57BL/6J mice, and then RSL3 (50 mg/kg) intratumorally administrated twice each week for two consecutive weeks. (b) Photographs of excised E0771 solid tumors (Scale = 1 cm). (c) Tumor weight, (d) relative reduction of tumor weight and (e) tumor growth of E0771 bearing mice ($n = 6$). (f) TLR2 protein expression in tumor tissues were detected by western blotting analysis ($n = 3$). (g) Immunofluorescence analysis of M1-like macrophages were monitored by F4/80 and iNOS double immunostaining in tumor tissues. The phagocytosis of tumor cells by macrophages in tumor tissues was observed and indicated by white arrow. Scale = 50 μ m (left panels) and 10 μ m (right panels). (h) THP1 macrophages were treated with SMU-Z1 (1 μ M, 24 h) and RSL3 (0.5 μ M, 6 h), and then phagocytosis was measured by flow cytometry ($n = 5$). The values are represented as mean \pm SD. The p -values were determined by one-way ANOVA with LSD post hoc test (c), two-way repeated measures ANOVA (e), or independent samples t -test [(d), (f), (h)]. * $P < 0.05$, ** $P < 0.01$, *** $P < 0.001$, ## $P < 0.01$, ### $P < 0.001$, @@@ $P < 0.001$.

Figure 8

See image above for figure legend.

Supplementary Files

This is a list of supplementary files associated with this preprint. Click to download.

- [Supplementaryfigures.docx](#)
- [Supplementarymethods.docx](#)